



National Library
of Canada

Bibliothèque nationale
du Canada

Acquisitions and
Bibliographic Services Branch

Direction des acquisitions et
des services bibliographiques

395 Wellington Street
Ottawa, Ontario
K1A 0N4

395, rue Wellington
Ottawa (Ontario)
K1A 0N4

Your file - Votre référence

Our file - Notre référence

NOTICE

AVIS

The quality of this microform is heavily dependent upon the quality of the original thesis submitted for microfilming. Every effort has been made to ensure the highest quality of reproduction possible.

La qualité de cette microforme dépend grandement de la qualité de la thèse soumise au microfilmage. Nous avons tout fait pour assurer une qualité supérieure de reproduction.

If pages are missing, contact the university which granted the degree.

S'il manque des pages, veuillez communiquer avec l'université qui a conféré le grade.

Some pages may have indistinct print especially if the original pages were typed with a poor typewriter ribbon or if the university sent us an inferior photocopy.

La qualité d'impression de certaines pages peut laisser à désirer, surtout si les pages originales ont été dactylographiées à l'aide d'un ruban usé ou si l'université nous a fait parvenir une photocopie de qualité inférieure.

Reproduction in full or in part of this microform is governed by the Canadian Copyright Act, R.S.C. 1970, c. C-30, and subsequent amendments.

La reproduction, même partielle, de cette microforme est soumise à la Loi canadienne sur le droit d'auteur, SRC 1970, c. C-30, et ses amendements subséquents.

Canada

**SHAPE MEMORY ALLOY
ACTUATOR WITH AN
APPLICATION TO A ROBOTIC EYE**

Danny Grant

Department of Electrical Engineering
McGill University

February 1995

A Thesis submitted to the Faculty of Graduate Studies and Research
in partial fulfilment of the requirements of the degree of
Master of Engineering

© DANNY GRANT, MCMXCIV



National Library
of Canada

Acquisitions and
Bibliographic Services Branch

395 Wellington Street
Ottawa, Ontario
K1A 0N4

Bibliothèque nationale
du Canada

Direction des acquisitions et
des services bibliographiques

395, rue Wellington
Ottawa (Ontario)
K1A 0N4

Your file *Votre référence*

Our file *Notre référence*

THE AUTHOR HAS GRANTED AN IRREVOCABLE NON-EXCLUSIVE LICENCE ALLOWING THE NATIONAL LIBRARY OF CANADA TO REPRODUCE, LOAN, DISTRIBUTE OR SELL COPIES OF HIS/HER THESIS BY ANY MEANS AND IN ANY FORM OR FORMAT, MAKING THIS THESIS AVAILABLE TO INTERESTED PERSONS.

L'AUTEUR A ACCORDE UNE LICENCE IRREVOCABLE ET NON EXCLUSIVE PERMETTANT A LA BIBLIOTHEQUE NATIONALE DU CANADA DE REPRODUIRE, PRETER, DISTRIBUER OU VENDRE DES COPIES DE SA THESE DE QUELQUE MANIERE ET SOUS QUELQUE FORME QUE CE SOIT POUR METTRE DES EXEMPLAIRES DE CETTE THESE A LA DISPOSITION DES PERSONNE INTERESSEES.

THE AUTHOR RETAINS OWNERSHIP OF THE COPYRIGHT IN HIS/HER THESIS. NEITHER THE THESIS NOR SUBSTANTIAL EXTRACTS FROM IT MAY BE PRINTED OR OTHERWISE REPRODUCED WITHOUT HIS/HER PERMISSION.

L'AUTEUR CONSERVE LA PROPRIETE DU DROIT D'AUTEUR QUI PROTEGE SA THESE. NI LA THESE NI DES EXTRAITS SUBSTANTIELS DE CELLE-CI NE DOIVENT ETRE IMPRIMES OU AUTREMENT REPRODUITS SANS SON AUTORISATION.

ISBN 0-612-05449-7

Canada

Abstract

A novel Shape Memory Alloy (SMA) actuator is presented. The SMA actuator consists of twelve thin NiTi fibers woven in a counter rotating helical pattern around supporting disks. Fibers woven in this pattern accomplish a high efficiency transformation between force and displacement. In this manner, the actuator overcomes the two main mechanical drawbacks of shape memory alloys, that being limited strain and limited cycle lifetime. Experimental results with two actuators operating in an antagonistic manner demonstrate the feasibility of the actuators for use in miniature robotic systems.

Further, a camera platform was constructed as an application for the actuators. The camera platform prototype orients a small CCD camera head, that supplies data to a foveated vision system. The three degrees of freedom pan, tilt, and torsion, are realized by four actuators in an antagonistic fashion. The camera support was manufactured using light weight plastic, including the use of plastic hinges to reduce the use of weighty bearings.

Control of the actuators is accomplished via a two stage switching feedback law that has its basis in sliding mode control theory. Essentially, the controller switches according to the sign of the error choosing which actuator is agonist and which is the antagonist.

Résumé

On présente un nouveau type d'actionneur utilisant les matériaux à effet de mémoire. L'actionneur est constitué de douze fibres tissées autour de disques de support selon un motif à double hélice, à pas inversés. Cet arrangement réalise de façon efficace une transformation force-déplacement. On peut dès alors contrer deux des inconvénients principaux d'origine mécanique de ces matériaux qui proviennent de la limite en déformation et du nombre de cycles. Les résultats expérimentaux produits avec deux actionneurs en configuration antagoniste démontre la faisabilité de systèmes robotiques miniatures utilisant ces actionneurs.

Ensuite, on applique ces actionneurs à la construction d'une plateforme orientable qui supporte une caméra CCD miniature pour former la partie mécanique d'un système de vision fovéal. Les déplacements d'élévation, d'azimut et de torsion, sont produits par quatre actionneurs en configuration antagoniste. La structure est construite d'un matériau polymérique léger incluant des charnières flexibles pour limiter le nombre de roulements.

La commande des actionneurs, du type commuté à deux étages, est basée sur la théorie de la commande en mode glissant. Le signal de commande est commuté selon le signe de l'erreur et sélectionne à tout moment l'actionneur agoniste et l'antagoniste.

Acknowledgements

There are always many unseen contributors to a thesis report. First of all, I would like to thank my supervisor Vincent Hayward whose ideas and advice have made this thesis possible.

My parents, Alfred and Ellen Grant, have contributed immensely to my entire life and during the time of this thesis was no exception.

I would also like to thank Don Pavlasek whose machining expertise has both instructed and aided me in the camera construction.

Thanks also go to the many people who helped to maintain my sanity during these academic years, especially Stamatia Gazetas, David Rudd, Doug Perry, Marc Devries, and Julie Gravel.

Finally I would like to thank the Natural Sciences and Engineering Research Council of Canada for their financial support.

TABLE OF CONTENTS

Abstract	ii
Résumé	iii
Acknowledgements	iv
LIST OF FIGURES	viii
LIST OF TABLES	xi
Claim of Originality	1
CHAPTER 1. Introduction	2
1. OVERVIEW	2
2. MOTIVATION	2
2.1. Current State of the Art	3
2.2. A Different Approach	4
CHAPTER 2. Background	6
1. SHAPE MEMORY ALLOYS	6
1.1. The Shape Memory Effect	6
1.2. Phases of NiTi	6
1.3. Phase Transition Temperatures	6
1.4. Phase Transformation Austenite to Martensite	7
1.5. Phase Transformation Martensite to Austenite	9
2. LIMITATIONS OF SHAPE MEMORY ALLOYS	10
3. HISTORY OF SHAPE MEMORY ALLOYS	12
3.1. Electric powered Actuators	12
CHAPTER 3. Shape Memory Alloy Actuator	15

TABLE OF CONTENTS

1.	SHAPE MEMORY ALLOY ACTUATOR	15
1.1.	Simplified Case	16
2.	DESIGN PARAMETERS	18
2.1.	Displacement Gain	18
2.2.	Weave Pattern	21
2.3.	Design space	24
2.4.	Construction	24
 CHAPTER 4. Controller Design		 26
1.	INTRODUCTION	26
2.	EXPERIMENTAL SETUP	27
3.	OPEN LOOP RESPONSE	29
3.1.	Actuation	29
3.2.	Varying Current Amplitude	29
3.3.	Varying Pulse Width	30
3.4.	Quasi-Linear Relationship	31
4.	CONTROLLER DESIGN	32
4.1.	Motivation	32
4.2.	Two Stage - Linear controller	34
4.3.	Two Stage - Constant Magnitude	36
5.	EXPERIMENTAL RESULTS	37
5.1.	Limit Cycle	37
5.2.	Two Stage - Linear Boundary Layer	37
5.3.	Two Stage - Constant Magnitude	39
5.4.	Effects of Load	41
5.5.	Disturbance Rejection	41
 CHAPTER 5. Camera		 43
1.	FOVEATED VISION SYSTEM	43
2.	GIMBAL AND SUPPORT	44
2.1.	Sensors	44
3.	ACTUATOR CONFIGURATION	46
4.	INTEGRATION	48
 CHAPTER 6. Conclusions		 51
1.	CONCLUSIONS	51
		vi

TABLE OF CONTENTS

1.1.	Future work	53
APPENDIX A.	Properties of NiTi	54
APPENDIX B.	Weave Patterns	55
REFERENCES		61

LIST OF FIGURES

2.1	SMA actuator configurations a) gravity as a bias force; b) spring as a bias force and c) antagonistic fiber pair	7
2.2	Matchbox model	8
2.3	Transition temperatures	8
2.4	Stress curve for Martensite	9
2.5	Stress curve for Austenite	10
2.6	Hysteresis in the strain-temperature relationship	11
2.7	Mollusk type - 2 dof gripper	13
2.8	Rotary joints	14
3.1	Shape memory alloy actuator	16
3.2	Simplified case: Two beams with two fibers	17
3.3	Displacement gain vs. weave pitch angle	17
3.4	Variables defined	19
3.5	Displacement gain vs. d and L	20
3.6	Inner bounding cylinder	21
3.7	Weave pattern for 5 notch actuator for $\gamma = 108^\circ$ and $\gamma = 144^\circ$	22
3.8	Unraveled fiber weave	22
		viii

LIST OF FIGURES

3.9	Completed weave	23
4.1	Top view of testbed	28
4.2	Open loop response to changing current amplitude	30
4.3	Open loop response to changing pulse width	31
4.4	Phase plot	32
4.5	Limit cycle	34
4.6	Two stage linear controller	35
4.7	Block diagram of two stage linear controller	36
4.8	Two stage constant controller	37
4.9	Limit cycle: Transient and steady state response	38
4.10	Step and ramp response of two stage linear controller	38
4.11	Step and ramp response of two stage constant magnitude controller	39
4.12	Block diagram of refined controller	40
4.13	Series of step responses	40
4.14	Effects of load	41
4.15	Disturbance torque	42
5.1	Foveated vision system	43
5.2	Hinge	44
5.3	Gimbal and support	45
5.4	Cross section of inner ring with bearing	45
5.5	Sensor operation	46
5.6	Sensor response	46
		ix

LIST OF FIGURES

5.7	Actuator sensor package	47
5.8	Actuator configuration	47
5.9	Paddles	48
5.10	Sensor actuator housing	49
5.11	Gimble motions	49
5.12	Integration of components	50
6.1	Shape memory alloy actuator	51
6.2	Camera prototype	52
B.1	Weave Pattern: 4 - notchs	56
B.2	Weave Pattern: 5 - notchs	57
B.3	Weave Pattern: 6 - notchs	58
B.4	Weave Pattern: 7 - notchs	59
B.5	Weave Pattern: 8 - notchs	60

LIST OF TABLES

1	Table of actuator configurations	24
2	Table of design tradeoffs	25
1	Feedback gains of two stage linear controller	36

Claim of Originality

The author of this thesis claims the following original contributions:

- the design of the shape memory alloy actuator prototype.
- the application of a variable structure controller to the SMA actuator and
- the design of the camera platform and components.

CHAPTER 1

Introduction

1. Overview

The focus of this thesis is the design, development and control of a novel light weight actuator utilizing thin fibers of the Shape Memory Alloy (SMA) nickel titanium. The applications of a powerful and compact light weight linear actuator are numerous, ranging from their use in toys to artificial organs. Our particular motivation for the actuators is in the design of a light weight, rapid camera platform as will be discussed in chapter one. Chapter two provides some necessary background information detailing the principles behind the Shape Memory Effect as well as a brief literature review on shape memory alloy actuators. The design of the actuator prototype and its various permutations are discussed in chapter three. The use of shape memory alloys dictates a non-linear control plant and hence the actuator proposed is inherently non-linear. A variable structure controller is applied to the actuator in Chapter four to handle these non-linearities. Chapter five details the construction of the camera platform, with the results further discussed in the conclusions in chapter six.

2. Motivation

As computational bottlenecks in image processing are overcome, the need for more active vision systems increases. Passive vision systems provide only one view of the world and therefore limit the amount of scene data available. An active vision system however is able to explore the visual environment, choosing areas of specific, task related, interest. This has a number of advantages, including: image stabilization, extension of the field of vision and a reduction in computational complexity [30]. Active vision systems are also required to take advantage of the benefits provided by foveated vision systems.

An integral part of any active vision system is the camera platform. In order to achieve the promising specifications that active vision systems can provide, compact, light weight camera platforms are needed. Such platforms are able to achieve high pan and tilt rates, as well as facilitate easy integration with other robotic systems. For example, such a camera platform could be mounted on the end of a robotic arm and positioned in space at a low energy cost. With this in mind, let us review the current 'state of the art' of camera platforms.

2.1. Current State of the Art. There exists to date a number of actuated stereo camera systems for research in vision. One of the earliest was built by R. Bajcsy at the University of Pennsylvania [2]. More recently, there has been designs constructed by the following institutions: the Royal Institute of Technology, Sweden [28], MIT [10], the University of Illinois [1], Harvard [7], the University of Rochester [4], the National Institute of Standards and Technology [34], and the University Toronto [21]. Similarly, single orienting platforms are being investigated at New York University [5], and Laval University [13]. It must be recognized that most of these earlier designs were developed for the purpose of exploratory research, so that in general, a particular emphasis on mechanical performance was of secondary importance.

A common characteristic to all these designs, except the NYU design, is that they implement off-the-shelf actuators (direct drive DC or stepper motors) and motion sensor components (encoders, potentiometers) fitted to custom design kinematic structures. Because typically, electric actuators have a comparatively small torque-to-weight ratio [3], these designs require torque amplification transmissions, via the use of gears, timing belts, or miniature harmonic drives with the resulting complexity and associated problems such as friction, wear and backlash.

The designs cited above, with the exception of the prototypes of Laval University, and of New York University, all fall in the category of gimbal arrangements with each stage of the gimbal being actuated separately. This approach results in cumbersome devices which all share the problems of serial manipulator designs, specifically: (a) geometrical growth of the actuator size and weight as we move from the distal to the proximal joints; (b) accumulation of errors in sensing and control; (c) non-uniform kinematic conditioning (this conveys actuator force mapping properties and sensing error amplification), which can only be made optimal in a narrow region at the center of the workspace; (d) poor dynamic performance due to rapid change of the inertial properties within the reachable workspace and (e) structural problems due to the need to support heavy actuators and to move them

rapidly. These problems are compounded with the problem of the weak torques available from electric motors. This is typified by the need to use a huge robot (Puma 760 at the University of Rochester) to position two miniature cameras.

Three devices are discussed somewhat further for purposes of comparison with our approach. The NIST design is interesting since by taking many short-cuts, it is capable of achieving impressive results in terms of agility and overall performance, and provides a rudimentary form of foveated vision. However, this is achieved at the price of monocular vision for a large field of view and absence of torsional motion. Actuation is performed with four costly direct drive electrical actuators which account for much of the performance, and the resulting device is a bulky machine weighting about 18 Kg.

The two other original designs, one from Laval and one from NYU are currently single platform systems. The Laval design also relies on conventional electric actuation, but the three actuators are grounded and the motion is transmitted by linkages arranged in a spherical configuration. This results in a rather bulky and heavy device which is delicate to manufacture owing to the exacting precision required by a vastly over-constrained mechanism. It is hard to imagine how such a device could be integrated into a compact head (two eyes with neck mobility) without a breakthrough in electric actuation which is unlikely to occur given the absolute limit set by field density in magnetic circuits. The NYU design is significantly more compact and relies on a moving magnet free to orient itself in a magnetic field induced by two pairs of Helmholtz coils. The current prototype suffers from under actuation which makes stabilization and rapid trajectory tracking difficult. Similarly, absolute limits set by the physics of magnetic circuits precludes any drastic progress. Moreover, by design it has only two controlled degrees of freedom which makes it impractical to consider the control of torsion motion.

2.2. A Different Approach. In order to realize a compact, light weight camera platform it would be ideal to have a powerful, compact, and lightweight actuator. Conventional techniques such as electric, hydraulic, and pneumatic actuators, suffer from a drastic reduction of the amount of power they can deliver as they scale down in size and weight [18]. To overcome this limitation, different actuator technologies have been investigated, in particular shape memory alloys. Shape memory alloys have a high strength to weight ratio which makes them ideal for miniature applications. A fiber of shape memory alloy can achieve a pulling force of 200 MPa. Comparing this to an electro-magnetic actuator, which can only achieve .002 MPa, this represents a 10^5 increase in strength per unit of

2. MOTIVATION

cross sectional area. Before considering an actuator constructed from shape memory alloys it is instructive to further examine some of the properties of this unique class of alloy.

CHAPTER 2

Background

1. Shape Memory Alloys

1.1. The Shape Memory Effect. Shape memory alloys achieve their actuation through the phenomenon of the 'Shape Memory Effect'. The NiTi alloy has two temperature dependent phases, or solid structural states. Essentially a fiber of NiTi can be pretreated to 'remember' a specific shape. In the low temperature phase, the Martensite phase, the alloy is quite malleable and can easily be deformed by external stresses. Upon heating, the alloy undergoes a phase transformation into the Austenite phase, regaining its original pretrained shape. Thus actuation occurs through an internal solid state restructuring of the material that is smooth, silent and powerful. Figure 2.1 shows how actuation is conventionally achieved with such a NiTi fiber. The fiber can be thought of as being trained to remember a specific length.

1.2. Phases of NiTi. There are actually three different phases of NiTi alloys, the Martensite, the Austenite and the R-Phase. The effects of the R-phase will not be considered to simplify subsequent analysis. A useful analogy to the two remaining phases of NiTi is given in Figure 2.2 where the atomic lattice of the NiTi is represented by matchboxes [32]. The Austenite phase has a cubic atomic structure and is represented by squares. The Martensite phase has a more rhombic structure and is represented by collapsed matchboxes or parallelograms. In actuality, the alloy changes phase in 3 dimensions with greater complexity, however the matchbox model gives a rough approximation of what is occurring.

1.3. Phase Transition Temperatures. The phase transitions of the alloy are characterized by four transition temperatures. They are:

- (i) A_s , the Austenite starting temperature,
- (ii) A_f the Austenite finishing temperature,
- (iii) M_s , the Martensite starting temperature,
- (iv) M_f the Martensite finishing temperature.

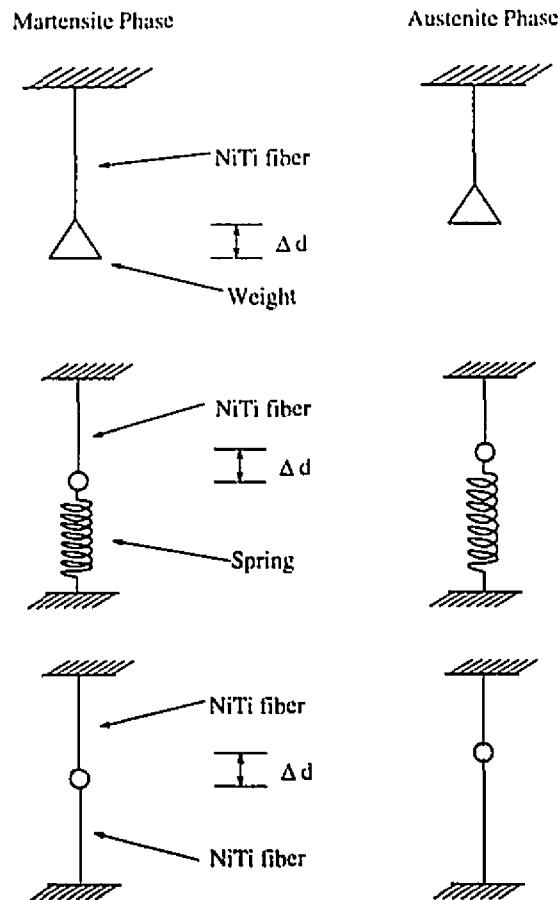


FIGURE 2.1. SMA actuator configurations a) gravity as a bias force; b) spring as a bias force and c) antagonistic fiber pair

Starting from a cool alloy (temperature/ $< A_s$) most of the atomic lattice is in the Martensite phase. As the temperature is increased beyond A_s , Austenite layers begin to form. When the temperature exceeds A_f the atomic lattice is mostly in the Austenite phase. Similarly, as the alloy cools, Martensite layers begin to form when the temperature reaches M_s , and the atomic lattice is mostly in the Martensite phase when the temperature is below M_f . Typically, hysteresis exists in the transition temperatures as shown in Figure 2.3.

1.4. Phase Transformation Austenite to Martensite. Using the match box example of Figure 2.2, we can see that as the Austenite cools, Martensite forms. Since the fibers used only exhibit the one way shape memory effect, there is no change in fiber length from this transformation. Instead the matchboxes collapse, leaning in opposite directions along subsequent layers. NiTi alloy in this form is said to be 'twinned' with each layer

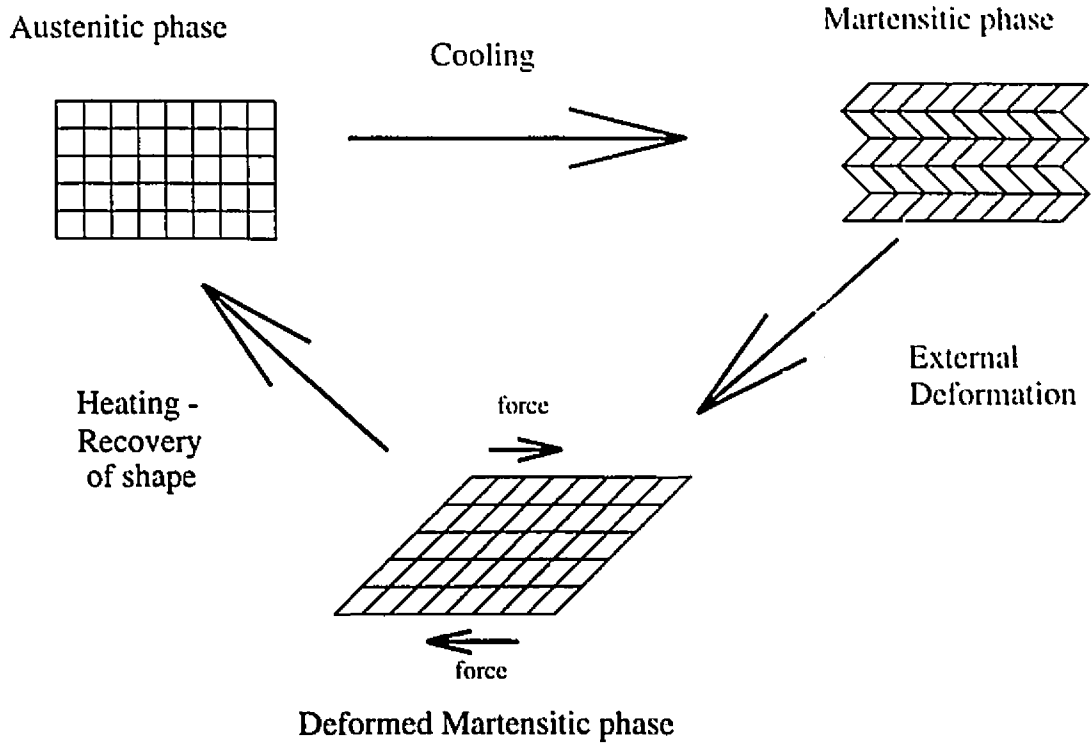


FIGURE 2.2. Matchbox model

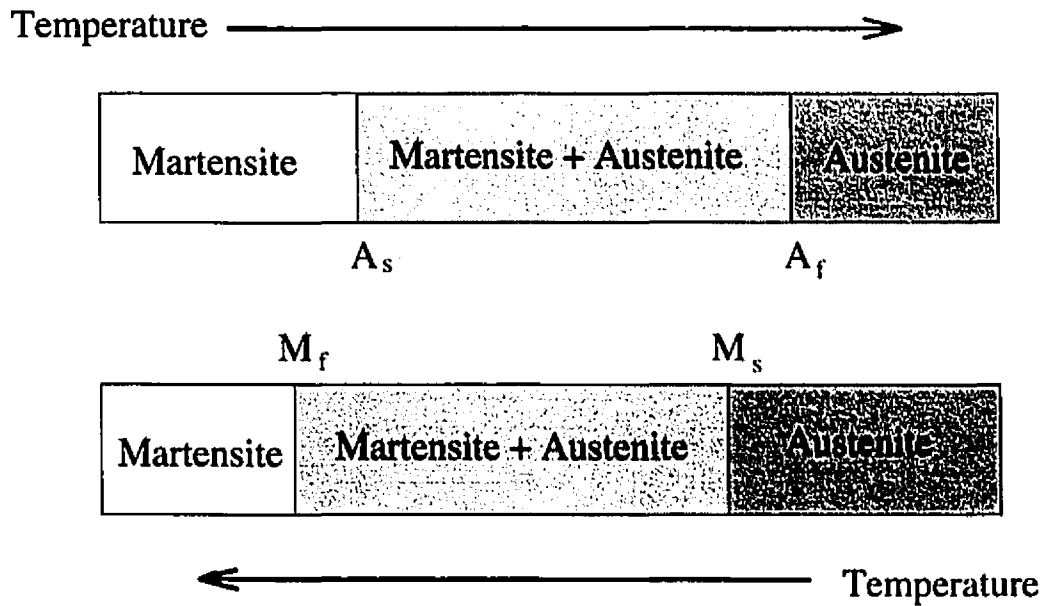


FIGURE 2.3. Transition temperatures

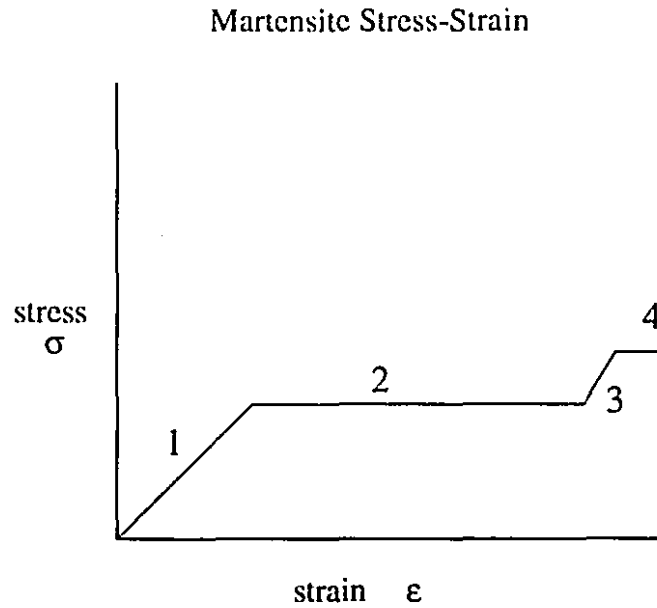


FIGURE 2.4. Stress curve for Martensite

separated by a 'twinning boundary'. The chemical energy is quite low along the twinning boundary, explaining why the alloy is quite malleable in this state.

Applying external stress to the Martensite will result in the stress-strain curve of Figure 2.4. The fiber initially behaves elastically with an associated elastic modulus as seen in stage one. Further external stress on the fiber will cause the Martensite layers to begin to lean in the same direction. When all the layers are leaning the same way the alloy is said to be 'detwinned'. This allows a large strain in the material with a small increase in external stress as seen in stage two. When the material is fully detwinned, the alloy again behaves elastically up to the point where the external stress begins to break the atomic bonds between Martensitic layers, and permanently deforms the alloy as seen in stages three and four.

1.5. Phase Transformation Martensite to Austenite. To recover the original shape of the NiTi alloy, it is necessary to add energy in the form of heat. The layers of NiTi crystals will line up into their pretrained form as the temperature exceeds A_s . In the Austenite phase, the alloy is rigid and can be likened to piano wire or hardened steel. Figure 2.5 shows the stress-strain curve of the alloy in the Austenite phase. The alloy behaves elastically for low stress (stage one) and is permanently deformed at higher levels of stress.

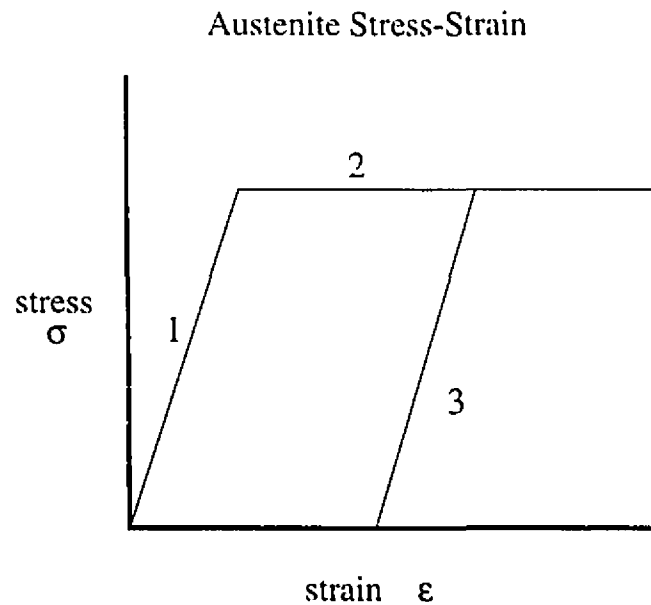


FIGURE 2.5. Stress curve for Austenite

Care must be taken to not exceed the deformation stress when the alloy is in the Austenite phase. External stress on the material also causes the four phase transition temperatures to increase. In this way it is possible to form stress-induced Martensite. If the alloy is in the Austenite phase and an external stress is applied that increases the Martensite starting temperature, M_s , above the current temperature, then Martensite will form. Since the alloy is now in the Martensite form it is malleable for a large percent strain. If the stress is then removed the transition temperature again decreases and the material reverts back into the Austenite phase. This has been termed 'superelasticity' in the literature.

2. Limitations of Shape Memory alloys

Although shape memory alloys appear to be attractive for robotic applications, they also come with some limitations. First of all, since their operating principle is based on a phase transition in a metal, they are highly non-linear. Properties such as the stress-strain relationship, internal resistance, latent heat of transformation, and thermal conductivity, are all phase dependent. A significant hysteresis is also present in the stress-strain relationship of the alloy as can be seen in Figure 2.6.

The second major limitation of shape memory alloys is efficiency. As mentioned in [18], the energy efficiency of shape memory alloy is theoretically restricted to approximately 10

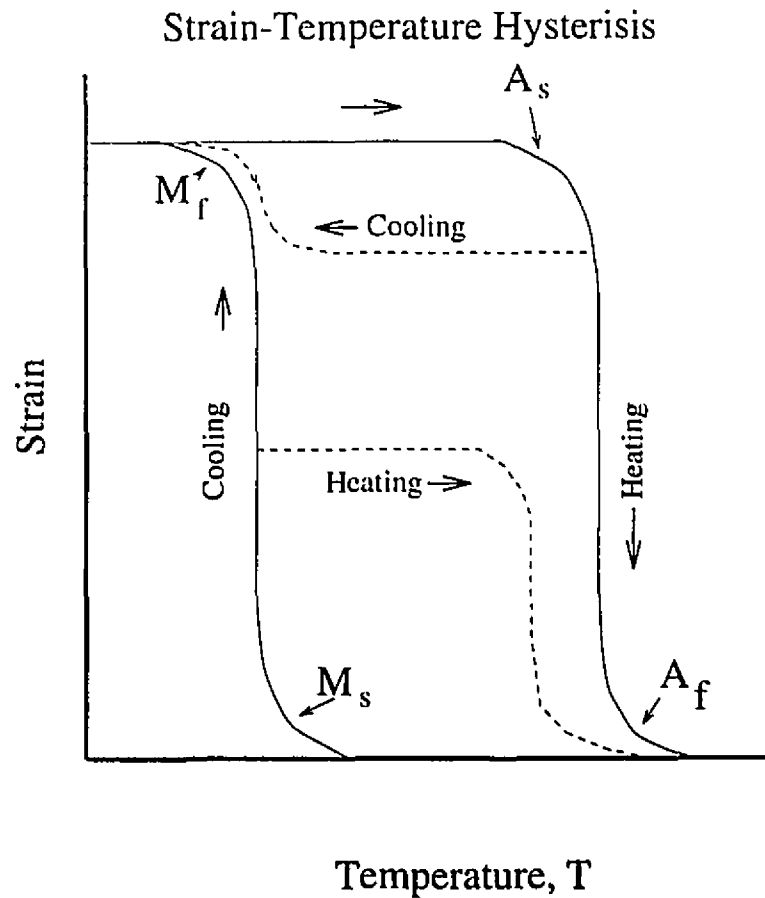


FIGURE 2.6. Hysteresis in the strain-temperature relationship

% by the Carnot efficiency cycle. Efficiency is often less than 1 % in practical applications, as the driving principle of the actuator can be considered as a heat engine operating at low temperatures. The applications of shape memory alloy actuators must be directed at areas where energy efficiency is not a concern.

Shape memory alloy's also have two major inherent mechanical limitations from the view point of actuation that are inter-related, those being limited percent strain and limited cycle lifetime. The absolute percent strain of shape memory alloys is approximately 8 %, with practical applications restricted to around 5 %. The lifetime of the alloy has also been found to dramatically increase if the fiber is operated at lower than absolute percent strain [18]. A cycle lifetime of 10^5 is reported in [17] at a strain of 5 %.

3. History of Shape Memory Alloys

The shape memory effect in alloys was first discovered by the Swedish physicist Arne Olander in 1932 using an alloy of gold and cadmium. Then in 1951 Chang and Reid used the gold and cadmium alloy in a cyclic weight lifting device at the Brussels World's fair that first demonstrated the feasibility of these alloys to perform useful work. Interest was sparked by their invention and soon many more alloys were discovered that exhibit the shape memory effect (SME). In 1961 at the U.S Naval Ordnance Laboratory, J.W Buehler discovered the SME in a NiTi alloy of 50/50 per cent composition. This gave the research interest a great boost as the new NiTi alloy, termed Nitinol, was both non-toxic and had a much lower manufacturing cost. By 1966 the study of Nitinol's chemical properties and crystal structure commenced in Japan resulting in the discovery of numerous more alloys that exhibit the shape memory effect as well as improvements in the manufacturing process of the NiTi alloy.

The early 1970's saw the emergence of several commercially available products that implemented shape memory alloys. Most of these applications were simple parts using a one time shape memory change such as pipe joints, stopping pins and clamps. A notable product at this time was the experimental artificial heart of Sawyer in 1971. The pump was electrically activated using pulses of current to heat the NiTi.

By the late seventies the Delta Metal company in England purposed several devices that operated more like mechanical actuators. They proposed devices to automatically open and close greenhouse windows, control water pipe valves for the hot water heating of buildings, and automobile fan clutches. Japan also had several commercial products available, notably the Matsushita Electric company's SMA controlled louvers in air conditioners in 1983 and Sharp's SMA controlled dampers in electric ovens. Additionally Nitinol alloys have found uses in such diverse products as dental alignment reformers, eyeglasses and brassiere frames.

3.1. Electric powered Actuators. In 1983, Honma, Miwa and Iguchi [16] demonstrated that movement in the shape recovery process of NiTi is controllable by electric heating and hence effective in the implementation in micro-robotics. Two actuator configurations were proposed. The first, a rotary joint, was used in their 'skeleton-muscle type' robot. The robot was a 5 dof arm consisting of an aluminum pipe skeleton operated with thin fibers (0.2 mm) and bias springs. The second actuator, used in their 'soft body type' arm, consisting of a thin NiTi fiber encased in a silicone rubber coat that acted as a biasing spring (see Figure 2.7).

3. HISTORY OF SHAPE MEMORY ALLOYS

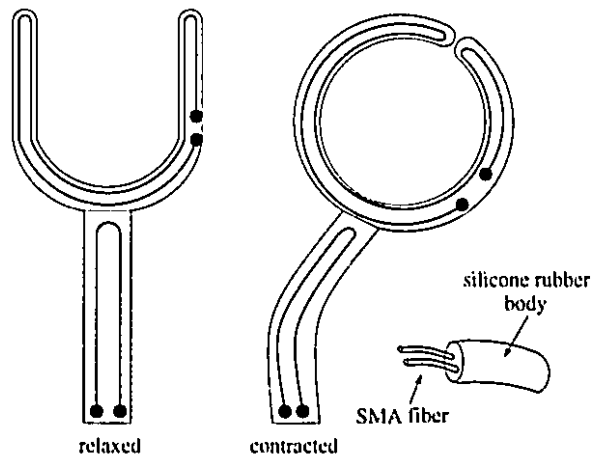


FIGURE 2.7. Mollusk type - 2 dof gripper

Hashimoto, Takeda, Sagawa, and Chiba [14] in 1985 extended this work and proposed two rotary joints, one operating with a bias spring and the other with two antagonistic shape memory alloy fibers. They applied the bias type actuator to a 6 dof biped robot and implemented heat sinks to improve the response time of the cooling cycle. They also validated the operation of the antagonistic actuator in the dynamic control of an inverted pendulum. Kuribayashi also proposed an antagonistic pair of fibers for the operation of a rotary joint in 1986 [22]. By implementing position and force controllers, he was able to validate a linear mathematical model for infinitesimal strains.

J.W. Walker proposed a rotary actuator based on torsionally strained SMA in 1987 [33]. Using the alloy to mechanically bias itself had the resulting advantage of eliminating the weight and bulk of a biasing spring. Micro-tongs were made (5mm x 1mm) to demonstrate the feasibility of his actuator configuration.

Several researchers have implemented shape memory technology for use in articulated hands. Notably Hatachi's (1984) four fingered robotic hand that incorporated twelve groups of 0.2 mm that closed the hand when powered. In 1987 Dario, Bergamasco, Bernardi and Bicchi [8] proposed an articulated finger unit using antagonistic coils and a heat pump.

Further miniaturized rotary joints were proposed by Kuribayashi using various shape memory alloy configurations as show in Figure 2.8. The configuration in Figure 2.8 part(f) was used to implement a *mm* size rotary joint that is driven by small bending beams of NiTi. This joint was also implemented in an articulated finger joint [23].

3. HISTORY OF SHAPE MEMORY ALLOYS

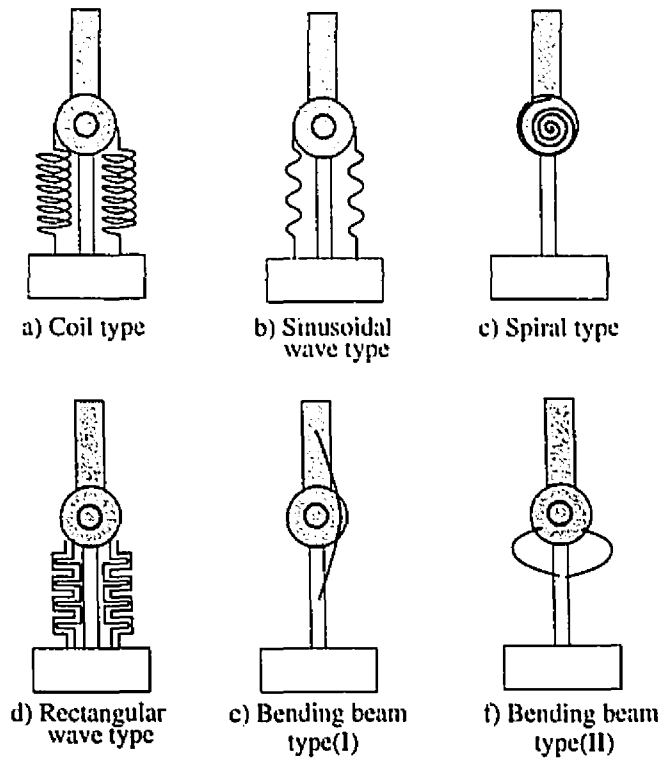


FIGURE 2.8. Rotary joints

CHAPTER 3

Shape Memory Alloy Actuator

The limitations of shape memory alloys can be overcome by either compensation via feedback or feed-forward controllers, or through better mechanical design. The non-linear properties of shape memory alloys are handled in this thesis by a variable structure controller that will be discussed in Chapter four. Efficiency is also not a major problem since our application involves using the actuators to drive a small light weight camera, essentially a miniature application. The remaining mechanical limitations must be overcome through design.

Many of the designs of actuators using shape memory alloys depend on mechanically amplifying the displacement either through the use of long straight fibers [14], [22], [29] or through the use of coils [17], [18], [22]. The actuator proposed in the next section overcomes the mechanical limitations of shape memory alloys, is more compact than a long straight length of fiber, and more efficient than using coils.

1. Shape Memory Alloy Actuator

The actuator, shown in Figure 3.1, consists of twelve thin NiTi fibers woven in a counter rotating helical pattern around supporting disks. The disks are separated by preloading springs that keep the fibers under tension when relaxed. When the fibers are heated, they contract pulling the disks together.

The weave pattern of the fibers accomplishes a high efficiency displacement amplification. Essentially the abundant force of the alloy is being traded off for a displacement gain. This transformation between force and displacement is highly efficient since the only loss in work is due to the slight bending of the fibers. Unlike shape memory alloy coils, the entire cross section of the fiber is performing work in the contraction. Coils suffer from the debilitating drawback of requiring a larger diameter than necessary. This is especially negative, when considering the response, since the response time is directly related to fiber diameter. A great deal of the material is wasted since, during the shape memory effect, only the skin of the coil is actually contracting at the maximum amount. The internal diameter

1. SHAPE MEMORY ALLOY ACTUATOR

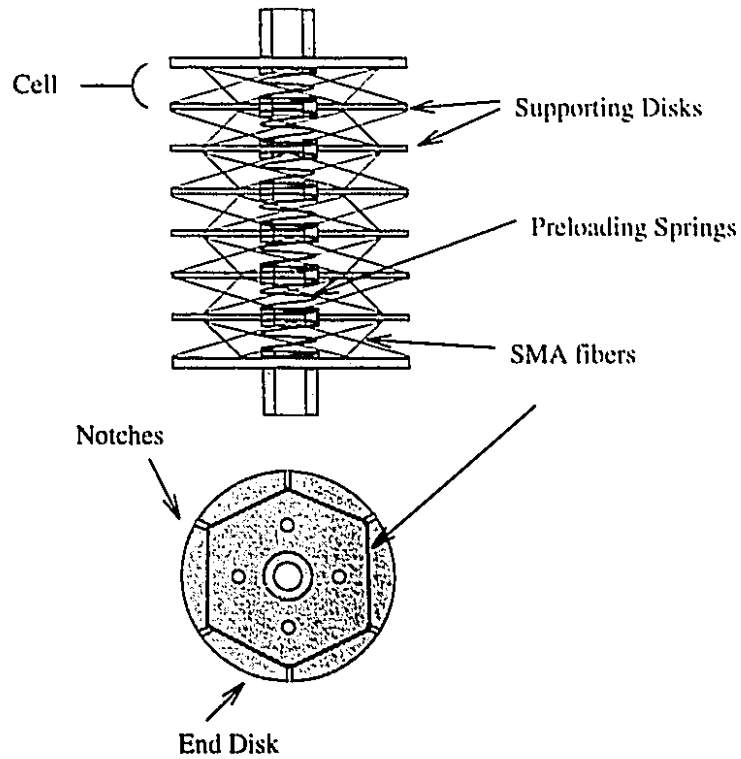


FIGURE 3.1. Shape memory alloy actuator

of the coil is acting both as a heat sink and as a producer of an opposing force to the desired motion.

1.1. Simplified Case. The kinematic amplification can best be seen by considering the simplified case consisting of two beams and two fibers as shown in Figure 3.2.

As the two fibers contract, the two beams are pulled together. The displacement gain, $\Delta d/\Delta s$, is defined as the change in stroke along the separating distance, divided by the change in the fiber length. Since ideally the motion is constrained along d we have:

$$s^2 = d^2 + L^2$$

$$\frac{\delta d}{\delta s} = \frac{s}{\sqrt{s^2 - L^2}}$$

but $s = L/\cos\alpha$, so,

$$(1) \quad \frac{\delta d}{\delta s} = \frac{1}{\sqrt{1 - \cos^2\alpha}} = \frac{1}{\sin\alpha}$$

1. SHAPE MEMORY ALLOY ACTUATOR

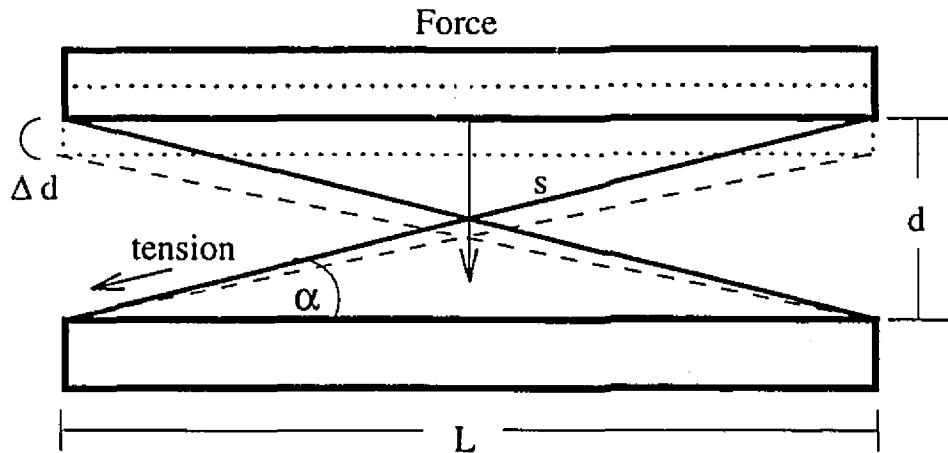


FIGURE 3.2. Simplified case: Two beams with two fibers

The displacement gain is inversely proportional to the sine of the weave pitch. As the disks get closer together the instantaneous displacement gain dramatically increases as seen in Figure 3.3 asymptotically approaching infinity.

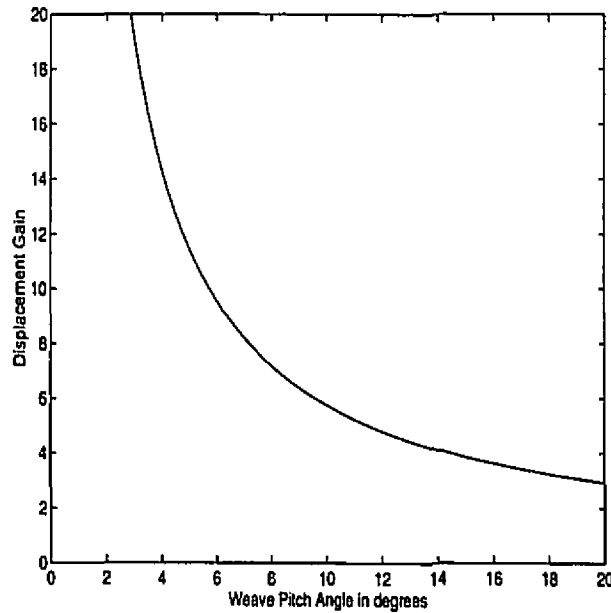


FIGURE 3.3. Displacement gain vs. weave pitch angle

Two fibers acting in such an arrangement have a gain in stroke at the expense of an attenuation of the traction force. Assuming the transmission between force and displacement

to be lossless, d'Alembert's principle gives us:

$$\Delta W = \Delta d \cdot F + \Delta s \cdot t = 0$$

hence,

$$\Delta d \cdot F = -\Delta s \cdot t$$

where t is the tension in the fiber and F is the force generated. The work performed by tensioning the fibers is equal to the work performed by the contracting disks.

The weave pattern of the actuator achieves a kinematic amplification for each cell of the actuator. All the radial components of the tension forces of the twelve fibers cancel, leaving only a common tensile stress force component. The displacement gain overcomes the two main mechanical drawbacks of the the alloy, while the force attenuation is compensated by using several fibers in parallel. The actuator is no longer limited to the absolute percent strain of the fiber. The displacement gain also allows the fiber to operate at reduced percent absolute strain. Since the cycle lifetime of the fibers increases dramatically if they operate at a lower than absolute strain, the cycle lifetime will also be increased.

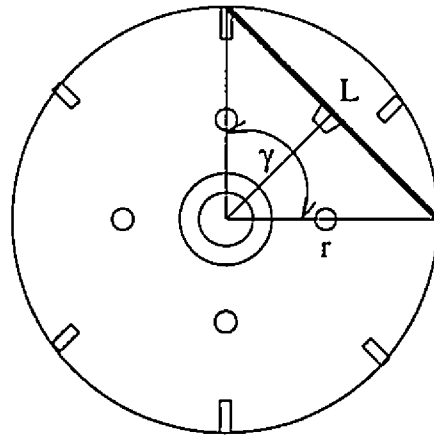
The weave pattern also results in an ideal 'tensegrity' structure [11], with all compression members being passive and all tension members active, resulting in an optimal use of the material. Loosely speaking, this has a biological analogy seen in the skeletal arrangements of creatures with endo-skeletons, where the muscles are the active tension members, and the bones are passive compression members.

The response of the actuator is limited by the cooling rate of the NiTi fibers, which directly depends on the fiber's surface area to volume ratio. The higher this ratio the more rapidly the fiber will cool. To obtain a reasonable response, one hundred micron fibers were chosen for the actuator prototype. Twelve 100 micron fibers acting in parallel, allow rapid cooling in ambient air without compromising strength.

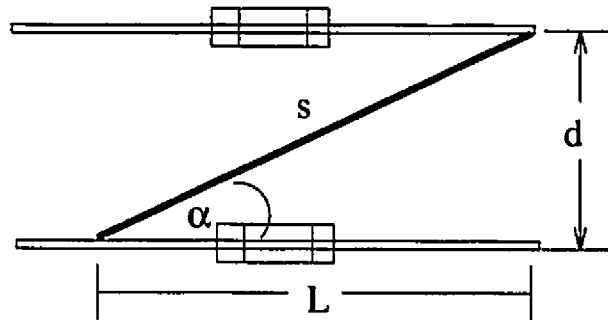
2. Design Parameters

The prototype represents only one configuration of the actuator's possible parameters. The supporting disk size and spacing, the number of fibers, and the displacement gain are all adjustable parameters. Figure 3.4 will define the variables involved, highlighting only one of the fibers in a single actuator cell.

2.1. Displacement Gain. All the parameters are inter-related leading to an engineering problem for which an acceptable trade-off must be found within set constraints. Equation(1) shows that the displacement gain is inversely proportional to the sine of the



Top View



Side View

- L** - length of fiber along disk
- r** - disk radius
- γ** - offset angle between successive disks
- s** - length of fiber
- d** - interdisk separation
- α** - weave pitch angle

FIGURE 3.4. Variables defined

weave pitch. The weave pitch in turn is dependent on the fiber weave pattern and the radius and spacing of the supporting disks. From figure 3.4 it can be seen that simple trigonometry gives us the following equation for the weave pitch:

$$\alpha = \arctan\left(\frac{d}{L}\right)$$

The weave pattern is determined by the number of notches around the disk, and the relative alignment of successive disks. The offset angle, γ , is the angle between notches of successive disks in the actuator. The length along the disk can be found by the following:

$$L = 2r * \sin\left(\frac{\gamma}{2}\right)$$

Putting all this together results in the following equation for the displacement gain.

$$\frac{\delta d}{\delta s} = \frac{1}{\sin\left(\arctan\left(\frac{d}{2r \sin\left(\frac{\gamma}{2}\right)}\right)\right)}$$

The displacement gain with respect to L and d is given by:

$$\frac{\delta d}{\delta s} = \frac{\sqrt{L^2 + d^2}}{d} = \sqrt{\frac{L^2}{d^2} + 1}$$

Figure 3.5 shows the displacement gain plotted against the separation distance d , and the length along the disk L , with a normalized radius.

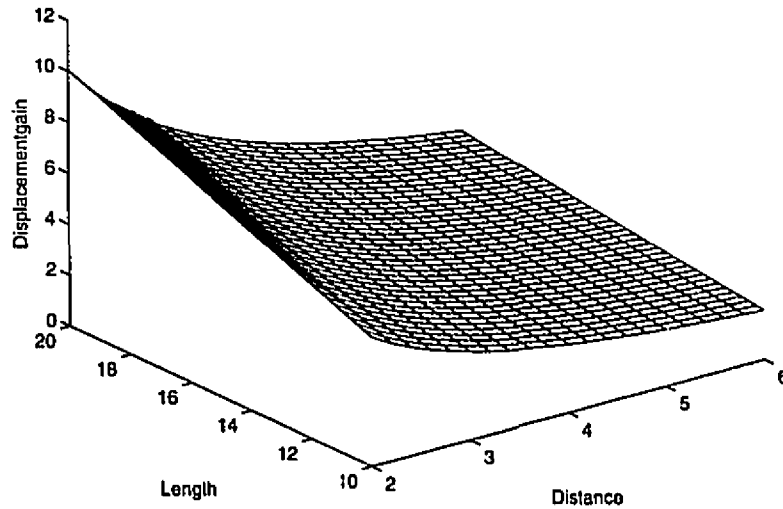


FIGURE 3.5. Displacement gain vs. d and L

2. DESIGN PARAMETERS

The displacement gain is augmented by increasing the offset angle γ , or by decreasing the inter-disk distance d . There are of course limits on both of these parameters. As the offset angle approaches 180 degrees, the fibers approach the axis of the disk. This causes the structure to become less stable and reduces the available space in the center for the placement of the springs and/or a position sensor, (an ideal place for a sensor). The radius of the inner bounding cylinder, shown in Figure 3.6 can be found by simple trigonometry to be $r_i = r * \cos \gamma$ where r is the disk radius and γ is the offset angle

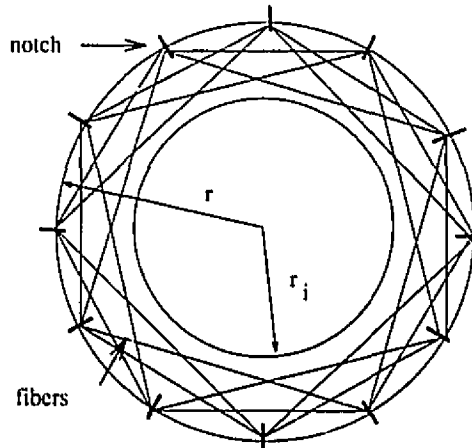


FIGURE 3.6. Inner bounding cylinder

Decreasing the distance in between the disks dramatically increases the displacement gain but limits the amount of stroke per cell. The minimum separation distance d , is then directly dependent on the weave pitch. If the disks begin their motion very close to one another they can only move a small distance before they come in contact with one another. The available stroke per cell can be increased by either increasing the offset angle or increasing the disk radius.

2.2. Weave Pattern. The weave pattern of the actuator determines how many fibers are to be used in parallel, and affects the displacement gain through the choice of the offset angle. Numerous configurations result in a stable weave that will operate much like the prototype (see Appendix B). For example Figure 3.7 shows the weave pattern of a five notch disk with two different offset angles. The top of Figure 3.7 has an offset angle of 108° with the notches of successive disks offset. The bottom of Figure 3.7 shows an offset angle of 144° with the notches of successive disks aligned. Note that as the offset angle is increased the inner bounding cylinder decreases.

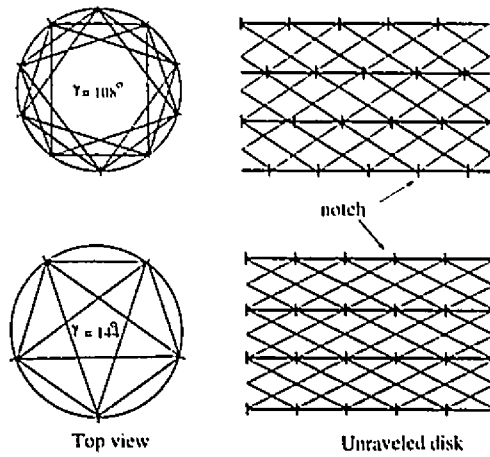


FIGURE 3.7. Weave pattern for 5 notch actuator for $\gamma = 108^\circ$ and $\gamma = 144^\circ$

For the actuator prototype in Figure 3.1, eight disks were chosen with 6 notches spaced 60° apart. The prototype actuator was constructed by aligning the disks vertically so that each successive disk was offset by 30° . The weave pattern was obtained by threading a single fiber along the notches of the eight disks. Adjacent disks were connected by the fiber through notches that were separated by an offset angle of 90° . The two end disks are woven along successive notches as shown in Figure 3.1. To get a better idea of how the fibers are woven, imagine the disks of the actuator rolled out so that they are flat. Figure 3.8 shows a four disk actuator with the disks unraveled. The fiber weave would begin at an end disk and pass through the successive points one through five.

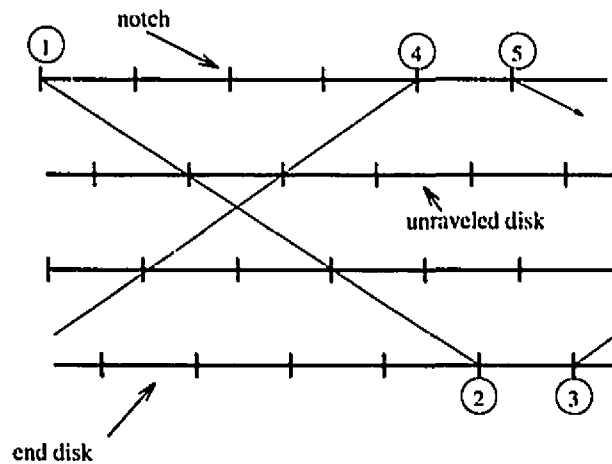


FIGURE 3.8. Unraveled fiber weave

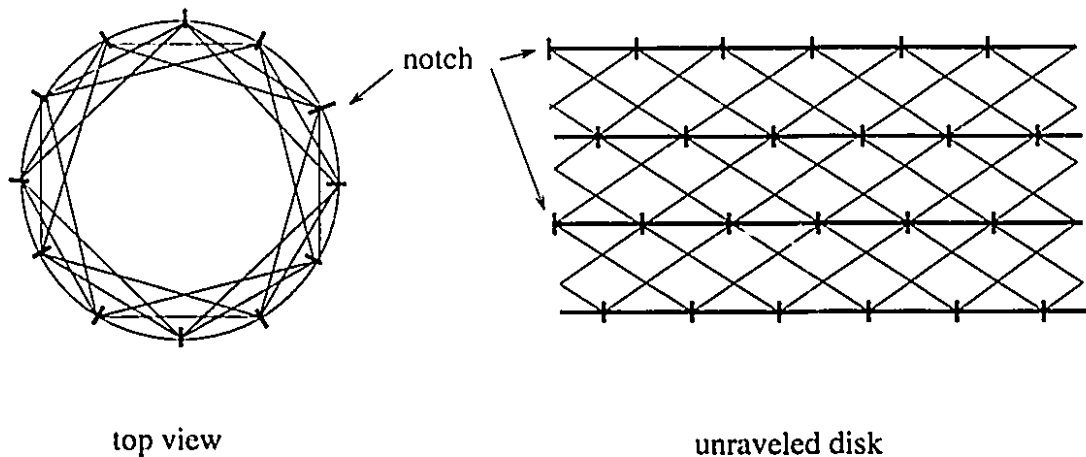


FIGURE 3.9. Completed weave

The fiber would then continue going back and forth between the two end disks until it arrived back at its starting position. The final result is twelve fibers woven in counter helical rotations such that all radial forces cancel out upon contraction.

Theoretically the weave pattern should be stable with an offset angle up to 180° . However configurations with an offset angle greater than 120° are not stable using the separating supporting disks. Configurations with a large offset angle tend to rotate into a lower energy configuration before heating due to unequal tension. This problem could be solved by using a support structure for the weave such that individual components are not free to rotate relative to one another. With the problems of friction aside, this could be accomplished with two or more guiding shafts along the disks. The actuator is completely modular in the sense that any number of cells can be cascaded together. Particularly long chains however will have difficulties with sagging unless an axial supporting shaft is used. To realize most of the weave patterns, a single fiber can be used with an odd number of actuator cells.

The force generated by the actuator can be adjusted by choosing the number and size of fibers used in the weave. Obviously, the more fibers that are acting in parallel the larger the force generated. Again there is a limitation here on the number of fibers that can be used. As the number of fibers increases so does the fiber interference in the weave. Fibers with a larger diameter can be chosen, but at the expense of response as cooling times will increase.

Table 1 shows a number of actuator configurations. The effect on the displacement gain is given by the length L , with a normalized radius.

Notches		# of fibers	Offset Angle	Length
num	angle		γ	L
8	45	16	67.5	1.111
			90	1.114
			112.5	1.663
7	57.5	14	86.2	1.367
			115	1.687
6	60	12	60	1.000
			90	1.114
			120	1.732
5	72	10	72	1.176
			108	1.618
4	90	8	90	1.114
			135	1.848

TABLE 1. Table of actuator configurations

2.3. Design space. The numerous configurations available result in a rich design space. A typical application for a miniature actuator requires a specific stroke length at a specific force. The overall size of the actuator is also often an important consideration. The actuator prototype was designed to have an initial displacement gain of five and a desired stroke of 2.5 mm. Since the actuator consisted of seven cells this corresponded to a 0.42 mm displacement per cell. The initial d was set at 2 mm to realize the displacement gain for an actuator with a radius of 7.5 mm. At full contraction, $d = 1.58$ mm the displacement gain was approximately seven. The actual fiber contraction was then approximately one per cent.

Table 2 summarizes the various tradeoffs in designing a shape memory alloy actuator.

2.4. Construction. The actuator prototype is hand woven. The supporting disks all have a threaded center so that they can be mounted on a threaded shaft. The disks are placed on the shaft alternately with the preloading springs. The proper alignment of successive disks was accomplished via guide holes drilled in the disks corresponding to the desired offset angle. For the actuator prototype, four guide holes were required offset by 90°. Once the support disks were mounted and the proper separation distance d , determined for the desired displacement gain, the disks were fixed to the center shaft by two nuts at each

2. DESIGN PARAMETERS

Desired property	How	Trade-off
Increase displacement gain	increase disk radius	increase in size
	decrease d	decrease in stroke per cell
Increase force	increase fiber diameter	slower response
	increase fiber #	increase in fiber interference
Increase stroke	increase weave pitch	decrease in displacement gain
	increase disk radius	increase in size
	increase # of cells	increase in size
Increase response	decrease fiber diameter	decrease in force
Decrease in size	decrease disk radius	decrease in displacement gain
	decrease # of cells	decrease in stroke

TABLE 2. Table of design tradeoffs

end of the actuator. The weave was then achieved by rotating the center shaft as the fiber was woven from end disk to end disk. In this manner it is possible to mechanical connect many fibers in parallel, quickly and securely. After the weave was completed the two ends of the fiber were merely tied in a knot. This also provided a secure mechanical connection as most of the stress on the fiber occurs at the notches.

CHAPTER 4

Controller Design

1. Introduction

A considerable amount of work has been undertaken with the modeling of shape memory alloy actuators [19], [9], [27], while relatively less attention has been paid to the design of feedback control laws. Many feedback control techniques reported in the literature applied to shape memory actuators are in fact linear compensators such as P, PI, PD or PID controllers [29], [27], or close cousins.

As seen in Chapter two, the dynamics of shape memory actuators are predominantly nonlinear because the energy conversion principle, from heat to mechanical, relies on exploiting phase transitions in a metal. This creates a significant hysteresis in addition to many other nonlinear effects having memory or not. In addition, the detailed properties of the dynamics of shape memory alloys vary greatly with their metallurgy, fabrication process, training techniques [17], aging, ambient conditions, and thus are difficult to describe accurately and in general terms. Moreover, most of the detailed descriptions of their underlying physics are often not very useful for controller design.

The overwhelming advantage of variable structure control is that relatively few parameters representing the knowledge of the physical properties of the plant need to be known since only inequality conditions need to be satisfied in the design [25]. It is also well known that variable structure control is quite insensitive to plant parameter variations since the resulting trajectory resembles a time near-optimal switching curve.

It is often stated that a disadvantage of VSS is the discontinuous nature of the control signal which may cause problems in actuators in terms of ringing, excessive dissipation, and excitation of unwanted dynamics in the plant being driven by these actuators. These problems sometimes can be minimized by the introduction of smooth switching laws while

retaining some of the advantages of the technique. Another approach is the introduction of boundary layers in the vicinity of the so-called sliding surfaces when the nature of the plant precludes the switching frequency to approach infinity, see for example [26].

For some actuation techniques, switching is not a problem and clearly shape memory alloy actuation is one of them: the mechanical energy is derived from heat which makes the actuators naturally low pass and thus undisturbed by step or impulse inputs. Moreover, the robustness properties of variable structure control combined with the modeling difficulties of shape memory alloy actuators creates considerable incentive to apply the former to the later.

One original motivation for variable structure control is that they are exceedingly practical [25]. No amplifiers, valves, or other continuous energy throttling mechanisms are required, only switches.¹ One great attraction of shape memory alloy actuators is the possibility for miniaturization. With variable structure control, the energy throttling device can be as simple as a single FET, switching current on and off from a power bus, thereby opening a path toward a mechatronic-type high degree of integration, including in a single unit actuation, sensing, control and energy throttling.

2. Experimental Setup

The fibers used in the actuator only exhibit the one way shape memory effect. For this reason it is necessary to force bias individual actuators so that they will return to their original length when cooled. This can be easily accomplished by using biasing springs or by using actuators in an antagonistic fashion. Shape memory alloys are especially suited to antagonistic arrangements since the force required to deform the alloy is about 1/5th of the force generated by the phase transformation [19]. The deformation stress is approximately 35 MPa while the recovery stress is near 190 MPa. Using the actuators in an antagonistic fashion also results in an improved system response since the response time of the actuator system will then strongly depend on the heat activation time constant, which can be tuned according to the input current amplitude. For these reasons open loop experiments were performed using two actuators in an antagonistic fashion. The testbed used for experimentation is shown in Figure 4.1.

The testbed consists of a pulley, mounted to a galvanometer shaft, and supports to connect the actuators mechanically and electrically. The galvanometer is a limited rotation

¹The energy throttling mechanisms often account for much of the complexity of systems, and robotic systems do not escape that rule as commented in [15]

2. EXPERIMENTAL SETUP

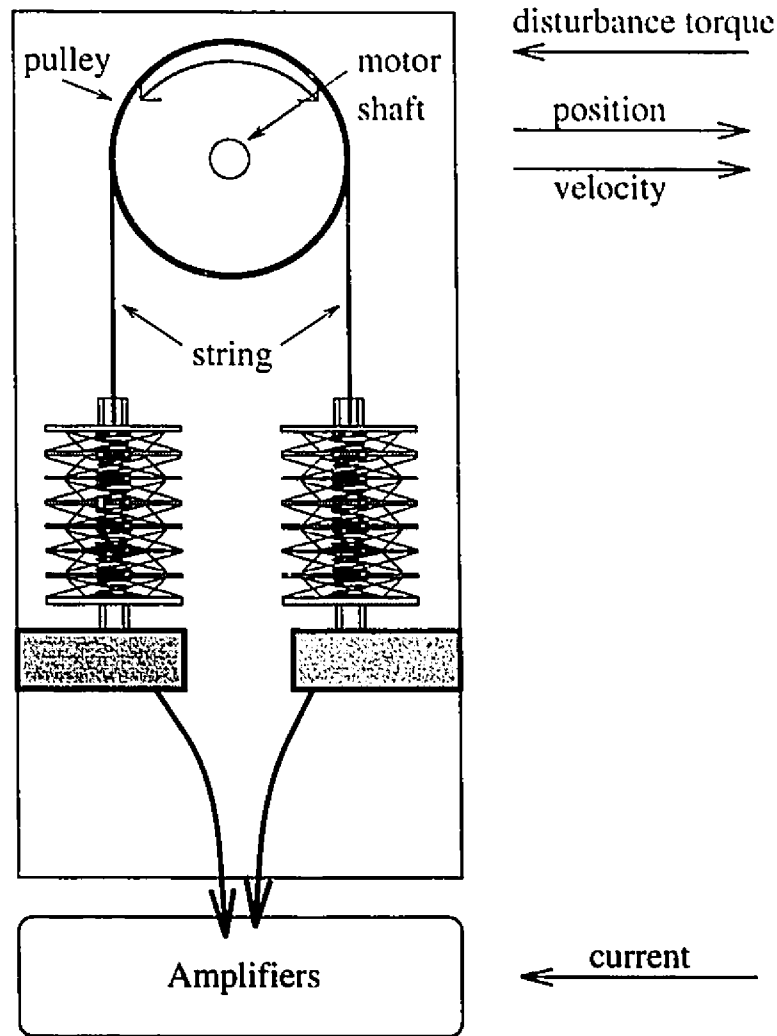


FIGURE 4.1. Top view of testbed

servo motor that is specifically designed for highly linear torque and deflection characteristics. The supporting controller board (the AE1000) comes complete with a PID controller, temperature compensation circuitry, and position and velocity sensors. For our experiments the testbed served as a highly linear position and velocity sensor, as well as a source of disturbance torque.

Position and velocity were measured by the galvanometer and fed through the A/D to a computer. Output signals included the motor current, used to simulate a spring-damper load, and control signals to pulse width modulate the fibers. Since the NiTi alloy is resistive it is possible to heat the fibers electrically. Heating was accomplished by using a

linear current amplifier that supplied constant current despite any changes in the actuator's resistance.

3. Open Loop Response

3.1. Actuation. Applying current across the end plates of the actuator cause the fibers to heat and contract. Actuation is accomplished in a smooth, silent and life-like fashion. In the ideal case all the radial components of force cancel leaving only a tensile force, resulting in an axial displacement. Also, in the ideal case, the separating disks would remain parallel, each anchor point on the disk being pulled equally. In practice this does not occur for two reasons. The first is that the supporting disks are made from aluminum, and aluminum acts as a heat sink causing the fiber to heat unevenly. The fiber near the supporting disks would be at a lower temperature than the fiber in between the supporting disks. This would cause them to contract at different rates. This does not occur in a symmetric fashion as the thermal contact between the fiber and the aluminum is not consistent depending on how much the fiber has contracted. The second reason is a result of the actuator construction. As the fiber is being wound onto the supporting disks it is likely that the tension in the fiber is not uniform.

This is not such a serious problem as would first appear due to the properties of the alloy. Sections of fiber that are under greater tension will have a higher Austenite starting temperature. This means that the sections of the fiber under lower tension will begin contracting before the sections of higher tension. This will act to cancel out any tension anomalies in a self regulating fashion.

The oscillatory behavior superimposed on the response is due to the linear under damped second order dynamics of the system accounting for load inertia, fiber elasticity and actuator damping. In the controller design, this effect has been ignored since it will be designed to track position and consequently will stiffen the system by a large factor.

3.2. Varying Current Amplitude. Open loop experiments were performed by using pulses of constant current to heat the fibers. Figure 4.2 shows the results of heating one of the actuators with a 50 ms pulse while varying the current amplitude by 0.5 A steps from 7.5 A to 14.5 A. Since the actuator consists of twelve fibers in parallel, the current in an individual fiber is divided by a factor of twelve.

Upon heating, the fibers initially undergo a small thermal expansion as can be seen in Figure 4.2 as a small displacement in the negative direction. This is followed by a relatively constant time lag as the temperature increases to the Austenitic starting temperature,

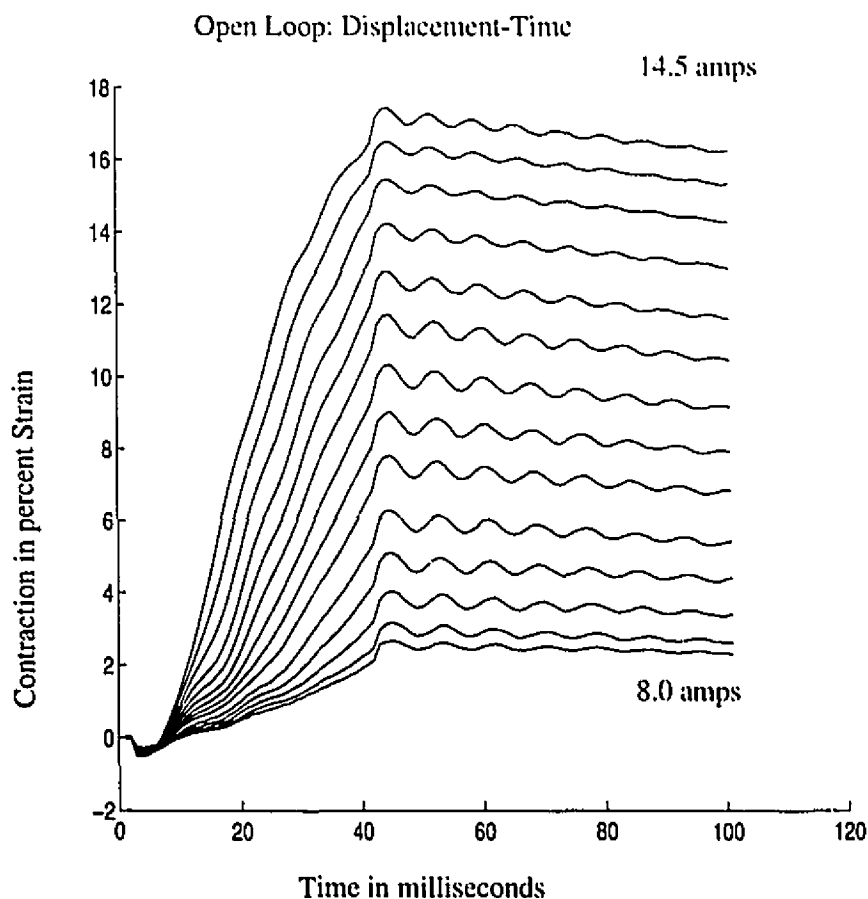


FIGURE 4.2. Open loop response to changing current amplitude

A_s . The phase transition then begins and the fibers begin to contract in an almost linear fashion. After the current pulse ends, the fibers undergo a thermal contraction and then expand according to the cooling time constant of the actuator. The oscillatory behavior superimposed on the response is due to the linear under damped second order dynamics of the system accounting for load inertia, fiber elasticity and actuator damping. In the controller design, this effect has been ignored since it will be designed to track position and consequently will stiffen the system by a large factor.

The initial time lag of the actuator depends on the temperature of the alloy when the current is applied. The time lag is relatively constant in this case since the alloy was allowed to cool to room temperature before a successive test was run.

3.3. Varying Pulse Width. Figure 4.3 shows the results of heating the actuator with a constant current and varying the duration of the pulse.

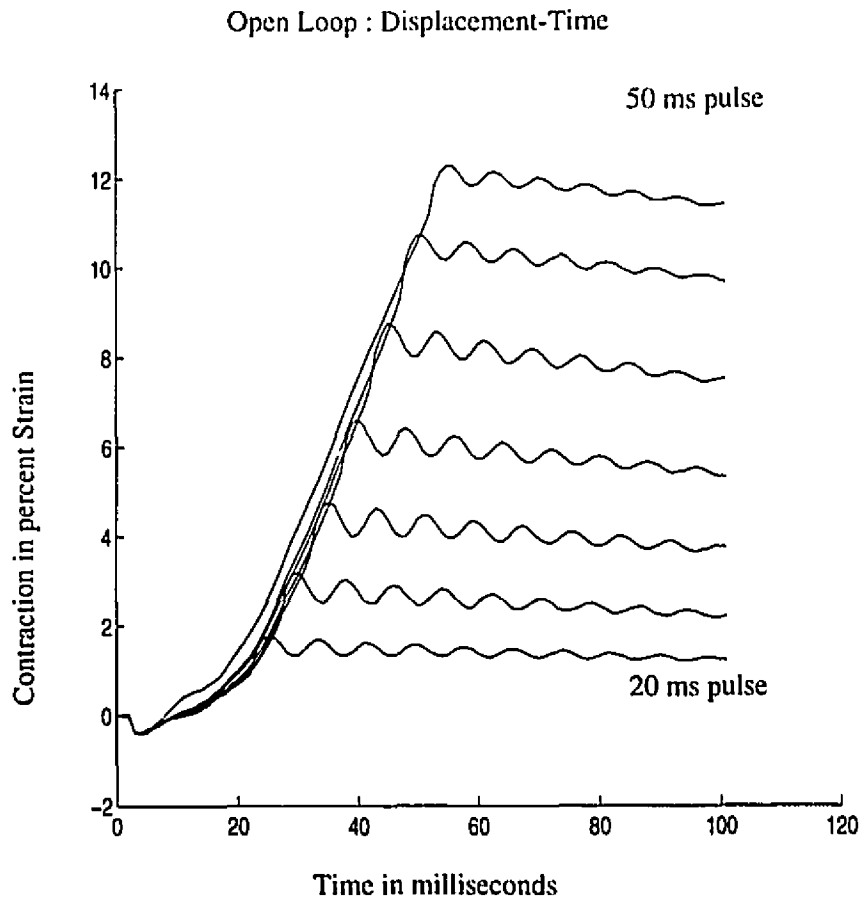


FIGURE 4.3. Open loop response to changing pulse width

Again the initial thermal expansion and time lag can be seen. The fiber then enters the phase transition and undergoes contraction in an almost linear fashion. This contraction continues as long as the current pulse is active, up to the maximum percent strain of the fibers.

3.4. Quasi-Linear Relationship. The open loop step response of the actuator reveals that although the phase transformations exhibit highly non-linear properties, a markedly linear relationship between heating time and percent strain can be observed in a large portion of the graph. This relationship occurs after the alloy's temperature reaches M_s , the Martensite starting temperature. Before that temperature is reached, the fiber undergoes thermal expansion which explains why the response appears to be "in the wrong direction" when heating is applied to a fiber significantly colder than M_s . This effect could

be approximated as a time delay, but can be ignored since when the actuator is under control for normal operation its temperature is kept in the vicinity of M_s .

The slope of the line depends monotonically on the magnitude of the current pulse used to heat the fiber. The higher the current the faster the temperature increase and therefore the faster the response. Again, the relationship between current magnitude and strain rate of change is quasi-linear.

Considering switching in time as a control signal, it is seen that the amount of displacement is in direct relationship with pulse duration and also in a monotonic quasi-linear relationship as exhibited by the final values of the family of curves.

4. Controller Design

4.1. Motivation. A switching control law makes it possible to drive the state trajectory of a non-linear plant along a user chosen surface in the state space. Such a surface is referred to as a switching surface since the control gain switches depending on whether the state trajectory is above or below the chosen surface. A position set point was chosen for the switching surface for the initial controllers. In the phase plot of position vs. velocity, this corresponds to a vertical switching surface at the desired position as shown in Figure 4.4.

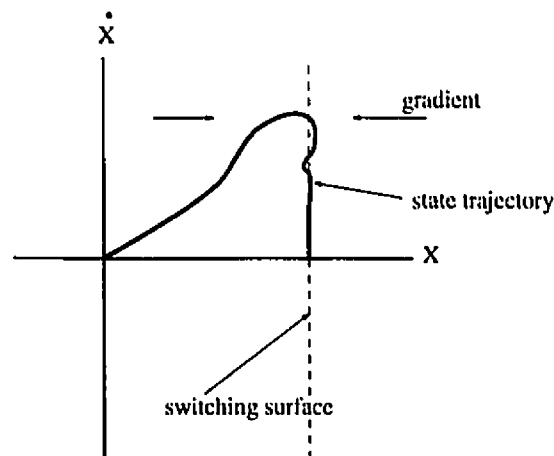


FIGURE 4.4. Phase plot

Starting from initial conditions, in this case the origin, the state trajectory is driven towards the switching surface. This is a result of constructing the control gains such that the gradient of the state space vector is always directed towards the switching surface. In the case of the antagonistic arrangement this merely entails switching the actuator according to the sign of the error. Also, note that the selection of which actuator is the agonist and

which is the antagonistic comes at no extra cost in the non-linear control design, whereas with a linear controller further adjustments are required.

With properly chosen feedback gains the state trajectory can be constrained to move along the switching surface after the initial intersection with the switching surface. Such a motion along a switching surface is referred to as 'sliding mode'. A sliding mode exists on a discontinuity surface, s , whenever the distance to this surface and the velocity of its change are of opposite signs [25]. More specifically:

$$\lim_{s \rightarrow 0^-} \dot{s} > 0 \text{ and } \lim_{s \rightarrow 0^+} \dot{s} < 0$$

Any perturbations from the switching surface results in an immediate control signal that forces the trajectory back on to the switching surface. Infinitely fast switching is required in order for the state trajectory to exactly follow the discontinuity surface. Actual systems however must always switch at a finite frequency due to various imperfections, such as hysteresis or delay. With well designed gains, the system will enter a limit cycle around the desired point in the phase plane.

In the time optimal sense, switching is the most efficient way to drive plants since the maximum realizable gain is used at all times. The major drawback of using maximum drive for high speed switching is stability. For small perturbations, the maximum feedback gain may cause the system to oscillate or to go unstable. The gain must be chosen so that it is large enough to drive the plant as quickly as required to the set point, yet be small enough so as to not cause oscillation larger than a specified limit. This oscillation near the switching surface is referred to as chattering. In the phase plane this results in the state trajectory going into a limit cycle as shown in Figure 4.5.

The top of Figure 4.5 shows a system that is sufficiently low passed such that the effects of switching can be ignored. This results in the state trajectory settling to the set point. The bottom of Figure 4.5 reveals the typical limit cycle, with the state trajectory oscillating around the set point at some finite frequency and some finite boundary layer.

Hybrid switching controllers have also been proposed [12], notably a two stage switching control law. In the two stage approach different feedback gains are used as one approaches the discontinuity surface. This results in a controller with several switching surfaces, however the surface defined by the set point is the only surface to exhibit sliding by the choice of the feedback gains. To achieve the desired performance specifications for the actuators, several two stage controllers will be implemented. When the position error is large the feedback gain will be the maximum, driving the plant as quickly as possible towards the

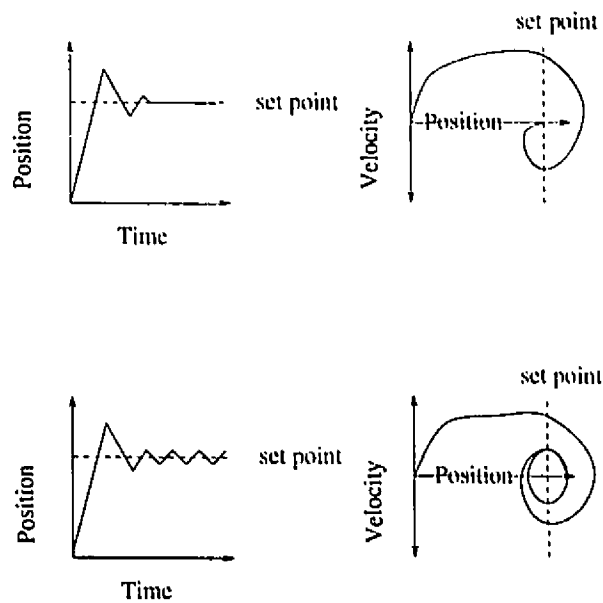


FIGURE 4.5. Limit cycle

set point. Once the plant's trajectory arrives within a specific layer of the set point the feedback control law switches in order to eliminate or reduce the level of chattering.

Limit cycles may be desirable in applications where the chattering is filtered out by the mechanics of the driven load. When possible, the existence of a limit cycle eliminates the steady state error due to the hysteresis in the actuator response and increases the average precision of the control acting like a self induced dithering signal. When its amplitude is kept reasonably low it may also have other beneficial effects such as linearizing the plant in the low frequencies and improving perturbation rejection. For the camera application discussed in Chapter five the limit cycle magnitude should be kept within a pixel of the CCD camera used. If a limit cycle is not desired, it is possible to consider a boundary layer around the discontinuity surface, inside which the plant is driven smoothly to the surface at the expense of time domain performance.

4.2. Two Stage - Linear controller. Figure 4.6 shows the three switching surfaces involved in the two stage linear controller. If the error is large then the maximum constant feedback gain is used. As the state trajectory approaches the set point the control is switched to the linear proportional controller.

This results in a smoother motion as the state trajectory slows down when it approaches the set point switching surface. The disadvantage of this, is that in the vicinity of the set

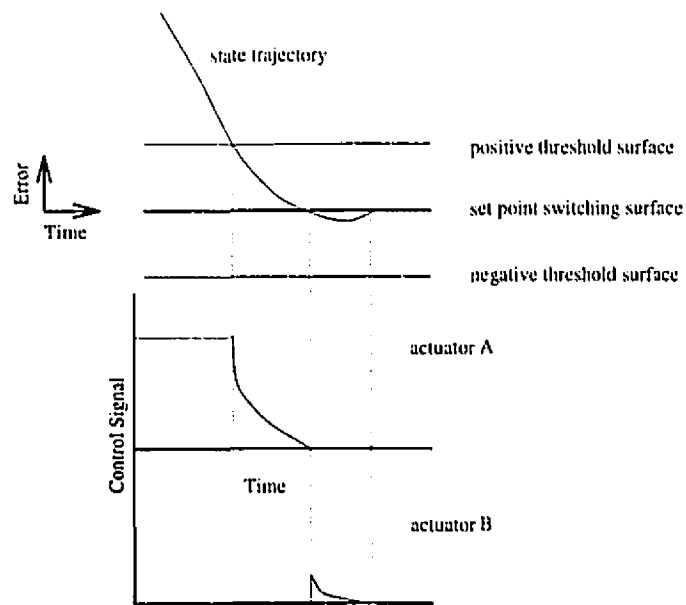


FIGURE 4.6. Two stage linear controller

point the feedback signal is low, so the plant is easily disturbed by small perturbations. A steady state error is also inherent in this controller, especially near the limits of the workspace.

The adjustable parameters for the two stage linear controller are:

- location of the threshold switching surfaces
- the amplitude of the constant current pulse
- the gain of the linear proportional controller

The amplitude of the constant current pulse should be chosen as large as possible in order to realize the shortest risetime. The limit here is not on how fast the fibers can be heated but on the stress generated by the actuators. Too large of a current pulse will overstress the actuator and have an adverse effect on cycle lifetime. The threshold switching surfaces should be placed as close as possible to the set point surface. However if they are placed too close the minimum energy delivered by the maximum constant pulse will be enough to drive the plant outside the boundary level. When this occurs the plant will go into a limit cycle with an undesirable large amplitude. Finally the gain of the linear proportional controller can be set as large as possible while maintaining stability.

Mathematically the control scheme is given by table 1.

The block diagram of the controller can be seen in Figure 4.7.

error signal	input
$error > \text{positive threshold}$	maximum positive constant
$\text{positive threshold} > error > 0$	$gain = k * error$
$0 > error > \text{negative threshold}$	$gain = -k * error$
$error < \text{negative threshold}$	maximum negative constant

TABLE 1. Feedback gains of two stage linear controller

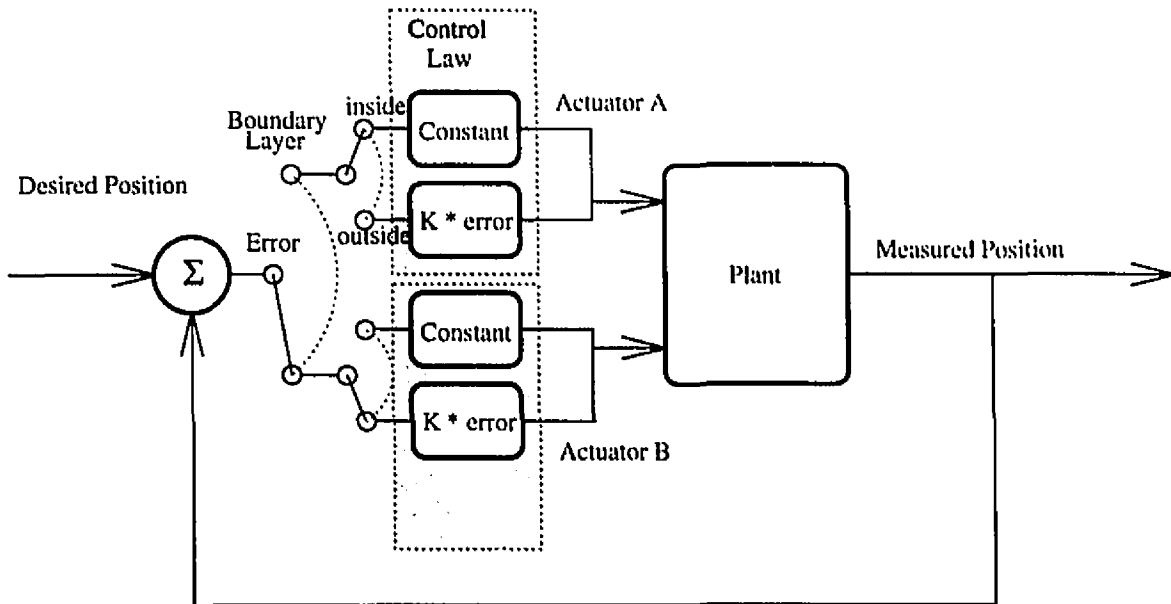


FIGURE 4.7. Block diagram of two stage linear controller

4.3. Two Stage - Constant Magnitude. The two stage constant magnitude controller is identical to the two stage linear controller except now a smaller constant input is used near the set point switching surface (see Figure 4.8).

This eliminates the need for a proportional amplifier to realize the control gain near the switching surface, simplifying amplifier construction. The controller should also be better able to resist perturbations as a significant control gain is applied for even a slight perturbation.

A good value for this gain near the set point is the current level needed to maintain the current temperature of the actuator. That is a current that will provide enough heat to compensate for the ambient heat loss. A limit cycle will result around the set point due to the time lag in the plant associated with the time delay in heating the fiber.

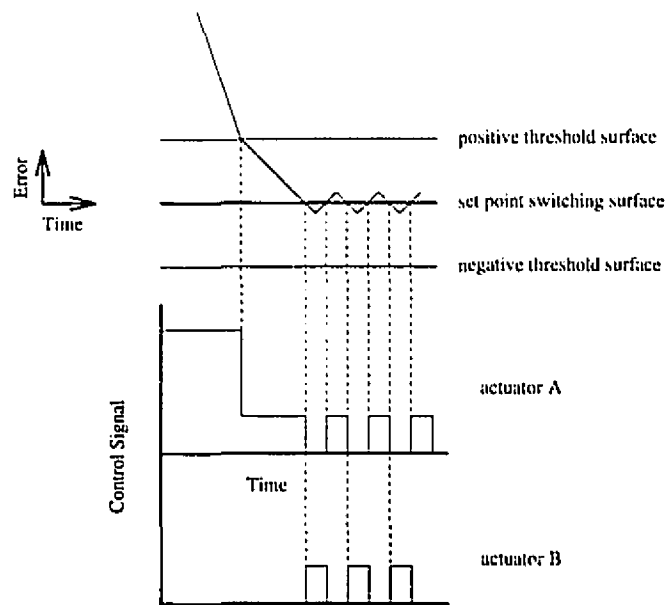


FIGURE 4.8. Two stage constant controller

5. Experimental Results

5.1. Limit Cycle. Figure 4.9 shows the existence of a limit cycle when a straight switching controller is used. The controller switches according to the sign of the error, with a constant feedback input of 9.2 A. The path in the phase plane for the steady state essentially forms a closed loop. Note that the overall length of the actuator used was 25 mm.

5.2. Two Stage - Linear Boundary Layer. Figure 4.10 shows the step and ramp responses of the two stage linear controller with the parameters set as follows: 1) maximum gain = 6 A; 2) linear proportional gain = $16.37 \cdot \text{error in A}$ and 3) threshold level = 0.25 mm. The various parameters have been tuned for the specific input step.

The step response, although smooth, never reaches the set point, and has a steady state error of 0.14 mm, due to the low feedback gain near the set point. Switching between the two actuators does not take place here since the plant's trajectory never reaches the sliding surface. The rise time, measured from the 10% to the 90% of the final value is, 87 ms with a 50 ms delay.

The tracking response has a time lag of 36 ms due to the delay between applied current and the phase transition. Also, note that the slight dip at the beginning of the ramp

5. EXPERIMENTAL RESULTS

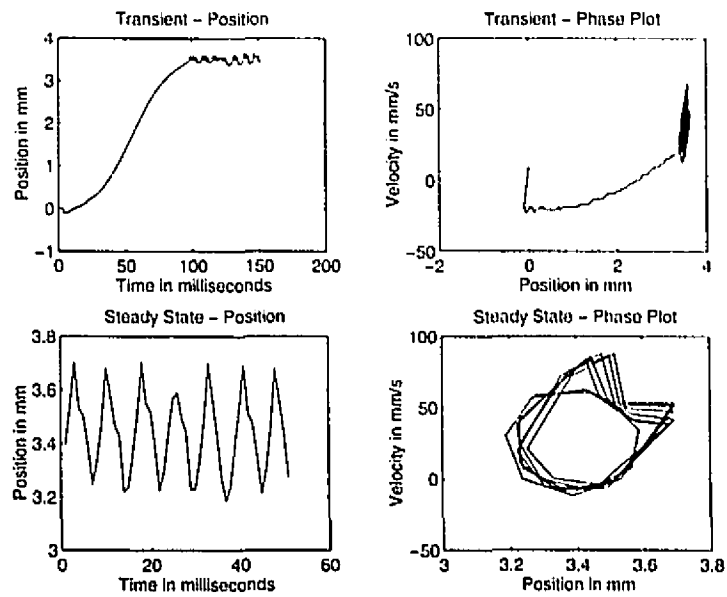


FIGURE 4.9. Limit cycle: Transient and steady state response

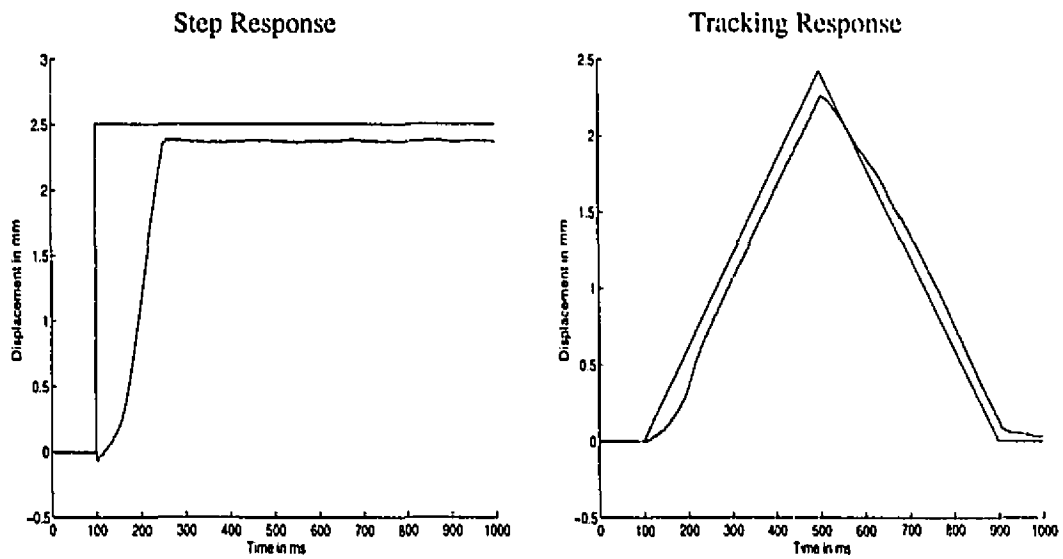


FIGURE 4.10. Step and ramp response of two stage linear controller

response is due to the fact that the actuator responds at a lower rate at the beginning of the phase transition as seen in the step response.

5.3. Two Stage - Constant Magnitude. Figure 4.11 shows the step and ramp response to the two stage constant controller with the parameters set as follows: 1) maximum gain = 6 A; 2) gain near set point = 4 A and 3) threshold level = 0.25 mm.

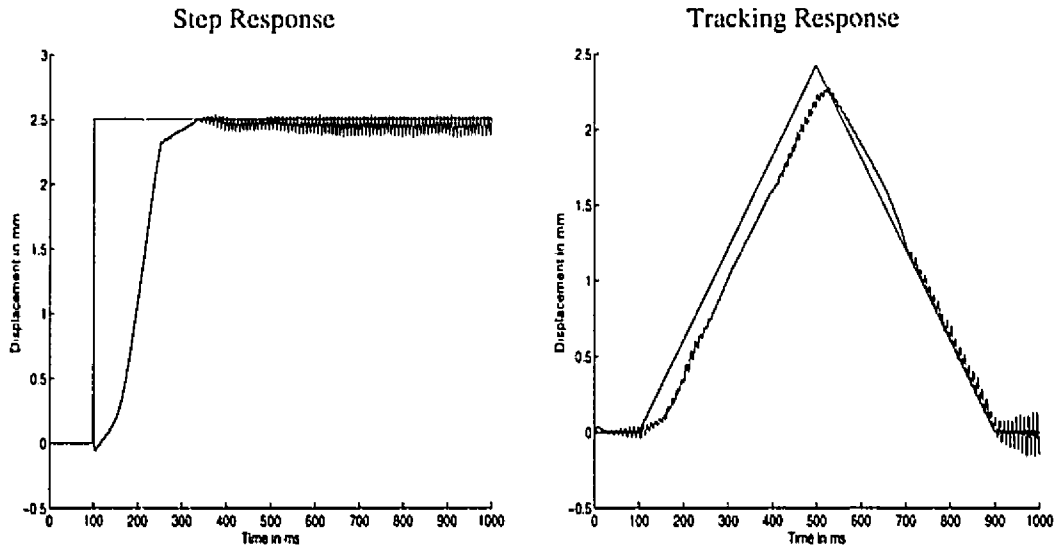


FIGURE 4.11. Step and ramp response of two stage constant magnitude controller

The step response here enters a limit cycle of 116 Hz with an average value steady state error of 0.04 mm. The rise time is 91 ms. The tracking response has a time delay of 28 ms for the positive slope and is nearly zero for the negative slope. This asymmetry in the tracking response is a byproduct of the displacement gain. As the actuator contracts the displacement gain increases. When the actuator is extended it has a lower displacement gain than when it is contracted. This means for the negative slope of the ramp the driving actuator will have a higher gain, and hence be able to follow the ramp more closely. This is also primarily why the two above controllers can only be ideally tuned for a small range of step response. As a refinement to the two stage constant magnitude controller, a different magnitude pulse was used inside the boundary layer, depending on the state space information, whether the actuator was extended or contracted. Again in an effort to keep the controller as simple as possible, a single magnitude was chosen for the feedback inside the boundary layer. The block diagram of the switching scheme is given in Figure 4.12.

The results of the refined controller can be seen in the series of steps show in Figure 4.13. The amplitude of the three pulses was set as follows: 1) high = 1.5 A; 2) medium = .95 A and 3) low = .55 A. Ideally the constant magnitude pulse inside the boundary layer should have an amplitude that compensates for the displacement force tradeoff throughout the

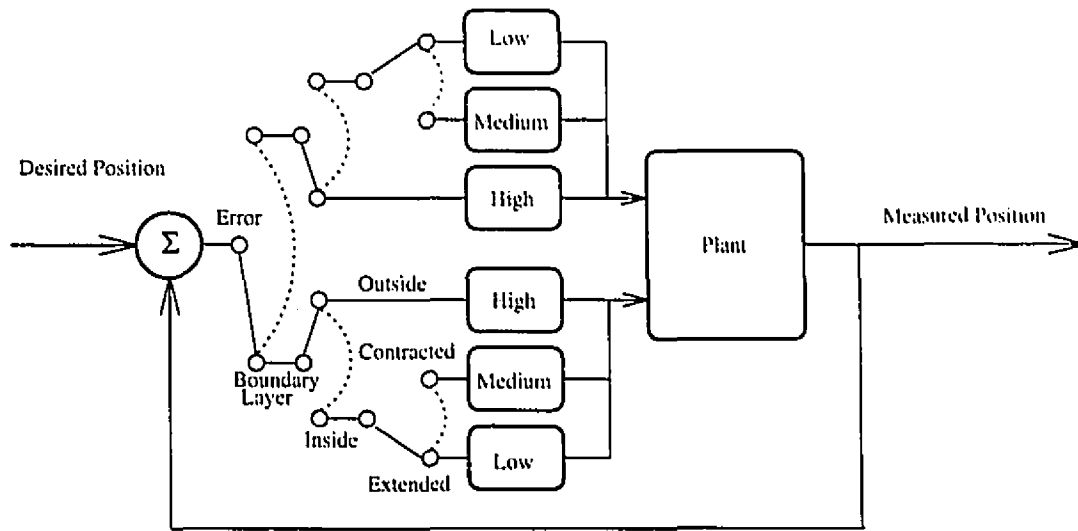


FIGURE 4.12. Block diagram of refined controller

Series of Steps

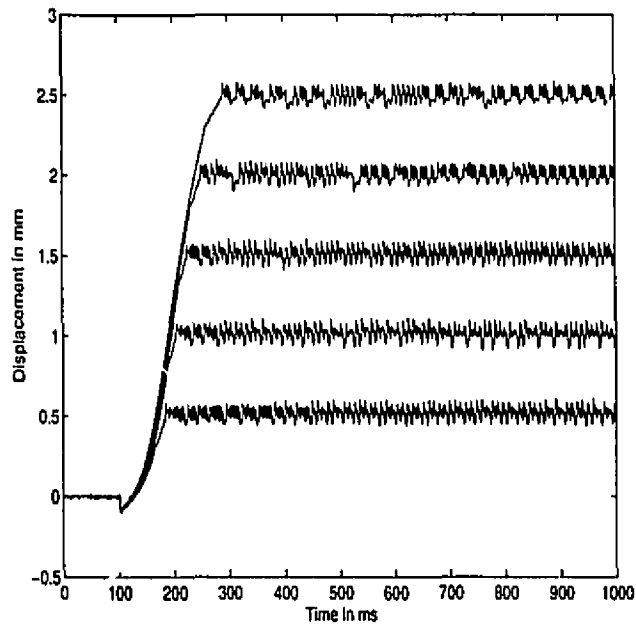


FIGURE 4.13. Series of step responses

workspace of the actuator. In Figure 4.13 the results of using only two magnitude pulses can be seen. For small steps, 0.5 mm, the limit cycle is slightly higher than the set point. The magnitude of the medium pulse is too high compared to the magnitude of the low pulse. However for large steps, 2.5 mm, the limit cycle is slightly below the set point. The

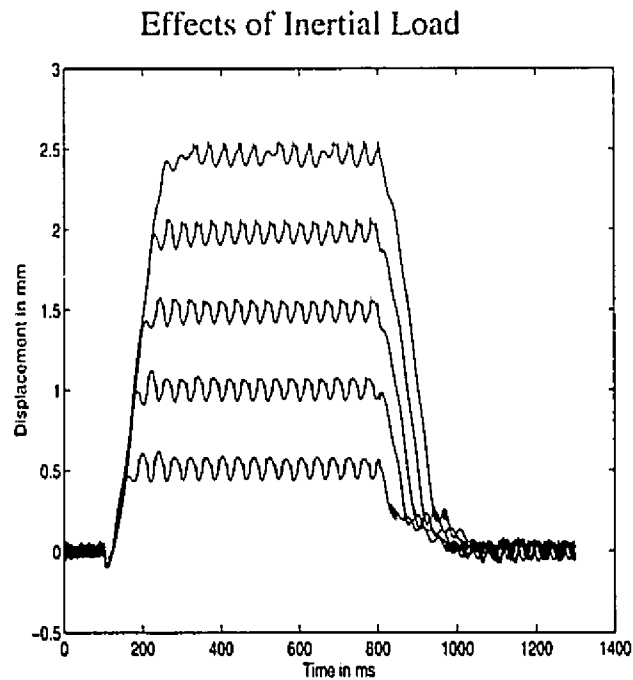


FIGURE 4.14. Effects of load

magnitude of the medium pulse is too low compared to the low pulse. And of course for the medium steps, the limit cycle is centered around the set point.

5.4. Effects of Load. Applying a load to the actuator system affects the limit cycle. The inertia of the mass causes the system to be lowpassed decreasing the frequency of the limit cycle. This can be seen in Figure 4.14 as a series of steps are applied to the system with an inertia of 1.08 kg/cm^2 .

5.5. Disturbance Rejection. By construction of the set point switching surface, any deviance from the set point results in an immediate gain that drives the plant back to the set point surface. In Figure 4.15 a disturbance torque step of $.03 \text{ Nm}$ is applied by the testbed at 100 ms . This corresponds to 1.0 N at the actuator or 25% of the actuator's maximum force.

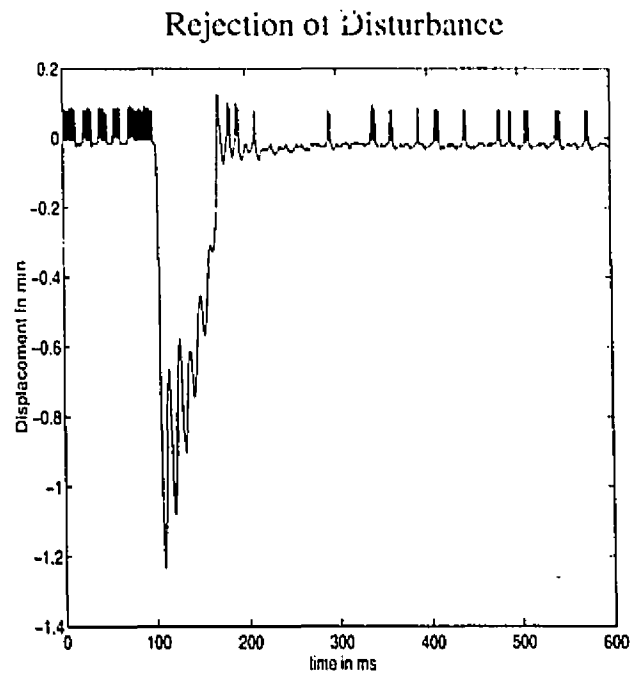


FIGURE 4.15. Disturbance torque

CHAPTER 5

Camera

1. Foveated Vision System

The camera platform was designed around a commercially available Panasonic camera, model GP-MS112. The model GP-MS112 features a 1/2" CCD with 335,000 picture elements in a compact lightweight package. The camera and lens assembly weigh approximately 50 grams. The need to orient the camera is motivated by the use of a foveated vision system based on a network of C40 DSP's [6], which consists of a high resolution fovea with eccentric circular overlapping receptive fields in the periphery as seen in Figure 5.1.

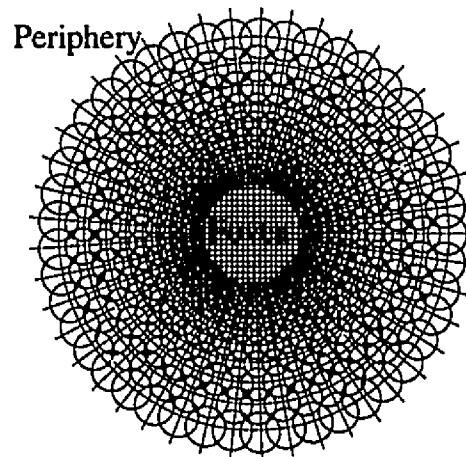


FIGURE 5.1. Foveated vision system

The resulting image output consists of two mappings. The fovea is a copy of the center of the image and each circle of the periphery corresponds to one output pixel and is mapped in log polar coordinates. The camera is required to pan and tilt to increase the field of vision. Torsion is required to simplify the processing of stereoscopic information in a two camera arrangement, or to compensate for camera motions.

2. Gimbal and Support

A gimbal arrangement was manufactured to support the camera. Essentially the gimbal consisted of an interior disk, suspended by an outer ring and supporting beams. The support structure was required to be light in weight, and as friction free as possible. In order to minimize the weight, the supporting structure was completely manufactured with durable light weight Delrin plastic. Friction was minimized in the gimbal by connecting adjacent rings with plastic hinges as shown in Figure 5.2 .

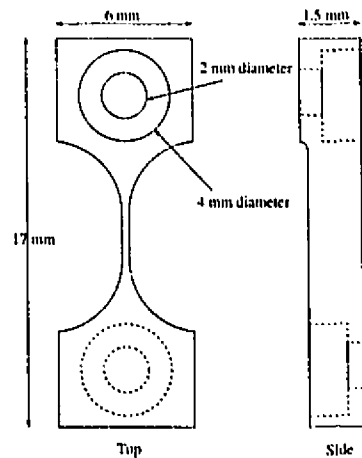


FIGURE 5.2. Hinge

The hinges have a flexible thin section in the center allowing the end points to rotate relative to one another. The entire gimbal arrangement can be seen in Figure 5.3. Torsion is achieved through the use of a thin section bearing embedded in the interior support ring of the gimbal. A retaining ring secures the bearing in place as shown in Figure 5.4.

2.1. Sensors. The two stage sliding mode controller requires position feedback in order to operate. Position sensing is achieved through the use of optical sensors at the end of the actuators. A support shaft was added to the actuator design to provide smoother motion upon actuation and to provide an essential component of the sensor. The support shaft was machined from Delrin, and was fixed to one of the end disks by a fitted hollow pin. The pin also provided a mechanical connection to the tendon. The optical sensor consists of a LED light bar and a simple photovoltaic cell. The support shaft then operates as a shutter between the LED and the photovoltaic cell as shown in Figure 5.5.

Moving the end disks relative to one another will cause the area illuminated on the photocell to change. The illuminated area on the photocell is linearly proportional to the

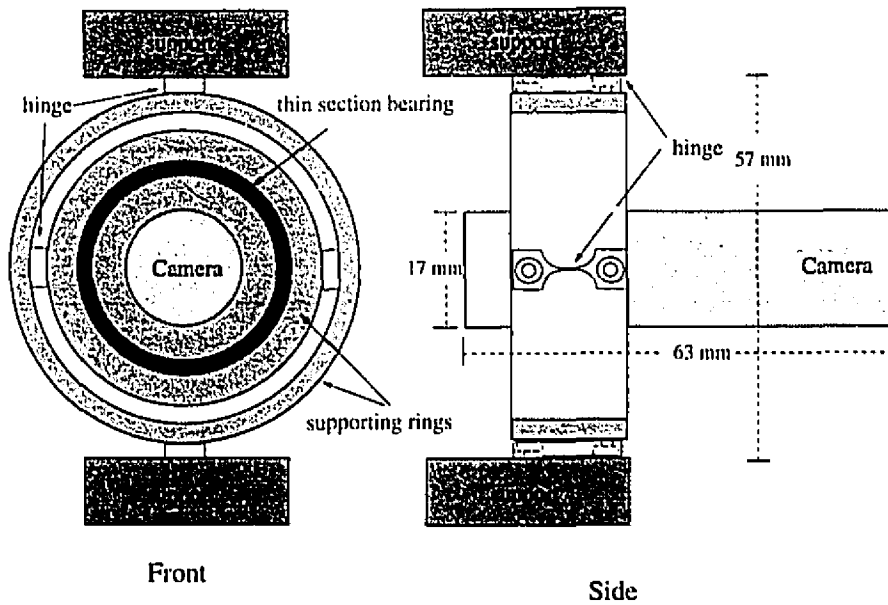


FIGURE 5.3. Gimbal and support

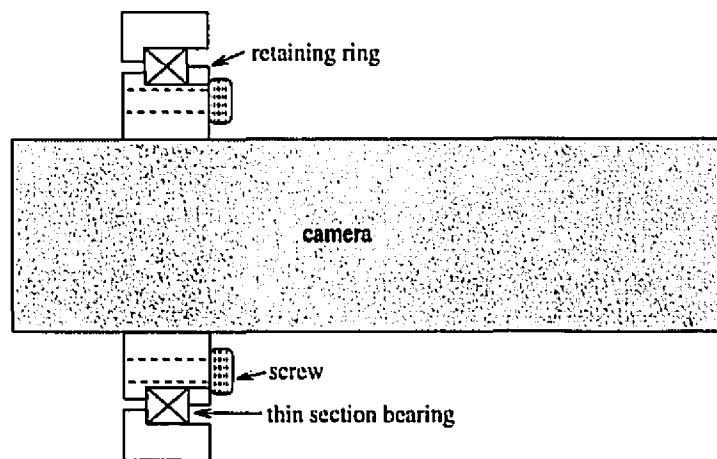


FIGURE 5.4. Cross section of inner ring with bearing

short circuit current of the photocell. A trans-impedance amplifier was then used to boost the signal from the photocell. The response of the sensor over its operating range is shown in Figure 5.6. The small bumps in the curve result from the fact that the light bar is actually four L.E.D's in an array, and therefore the light emitted is not completely uniform.

This provided us with a compact linear optical sensor that is easily integrated with the actuator (Figure 5.7). The housing of the sensor is also used to mechanically support the actuator and to fix the actuator at one end through a set screw.

3. ACTUATOR CONFIGURATION

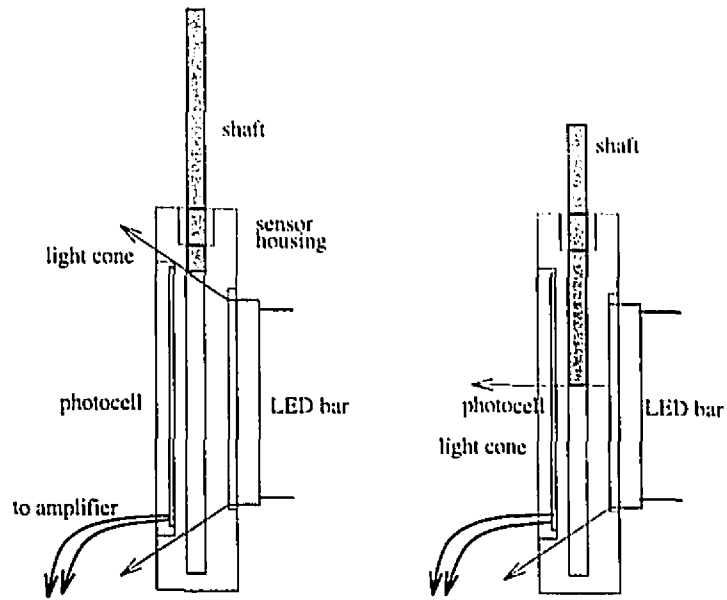


FIGURE 5.5. Sensor operation

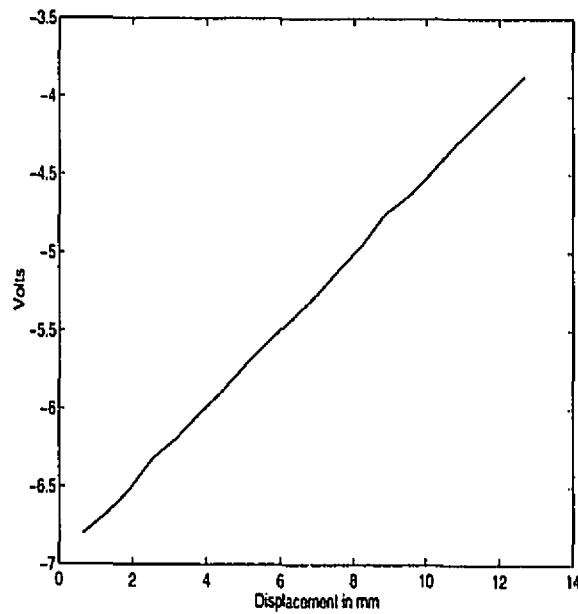


FIGURE 5.6. Sensor response

3. Actuator Configuration

Actuation of the camera platform is achieved through four actuators configured in a parallel arrangement. Parallel mechanisms are normally lighter in weight than serial

3. ACTUATOR CONFIGURATION

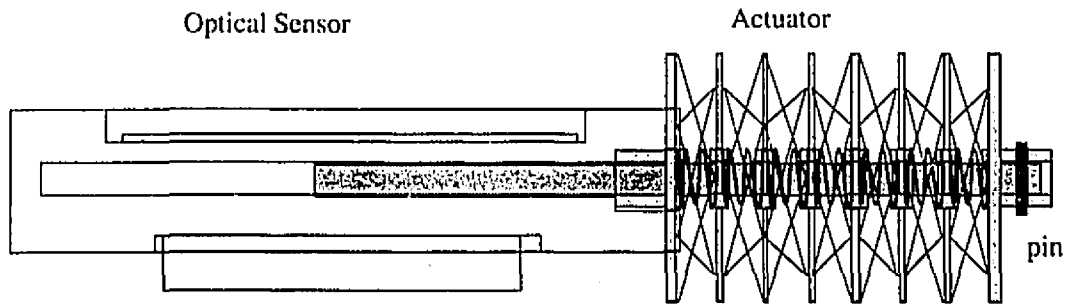


FIGURE 5.7. Actuator sensor package

mechanisms due to the pyramidal effect of serial mechanisms. The actuator configuration used is similar to that proposed in [24]. The interior ring of the gimbal has four anchor points that form a square. The configuration involves positioning the actuators in two pairs, each pair having a common base point, as seen in Figure 5.8.

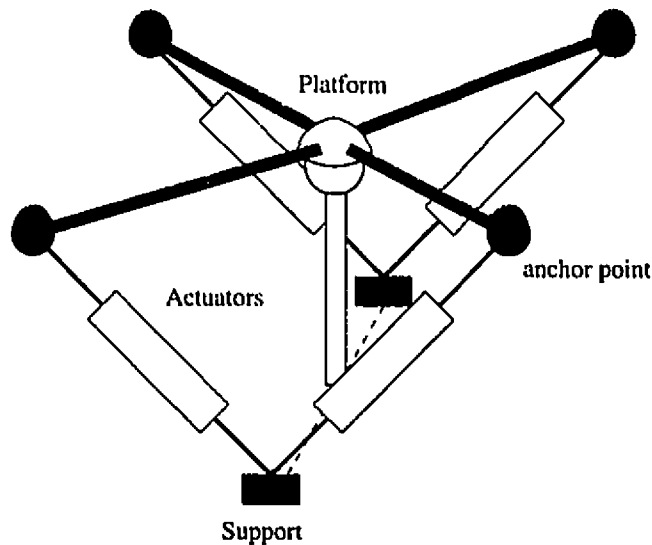


FIGURE 5.8. Actuator configuration

This increases the workspace of the system since collision between actuator pairs is avoided. Also in order to realize a more compact design, the passive gimbal is manipulated through the use of tendon drives. Paddles are used to connect the actuators to the gimbal through the tendons. This allows us to realize the physical arrangement of Figure 5.8 and to position the base of actuation for the pairs of actuators close together. Figure 5.9 shows how the four paddles are arranged. The paddles rotate around two smooth steel shafts supported by two cross beams. The tendons are connected to the gimbal through

the paddles and back to the actuators. Also note that the paddles implement an additional mechanical displacement gain.

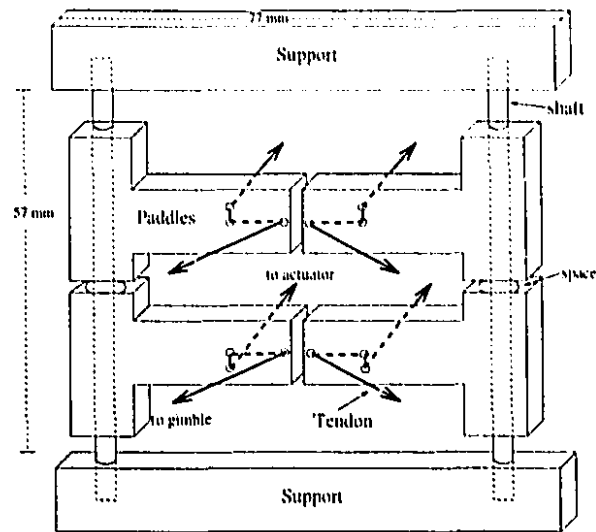


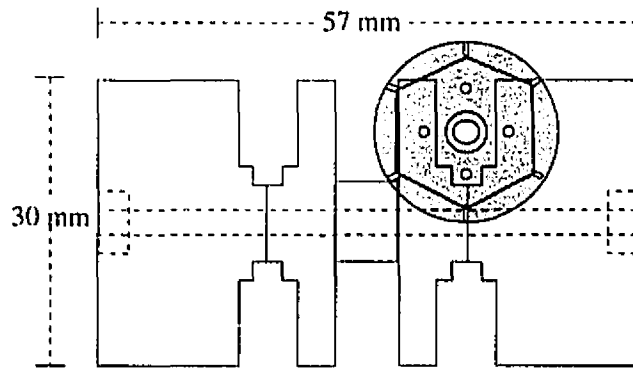
FIGURE 5.9. Paddles

4. Integration

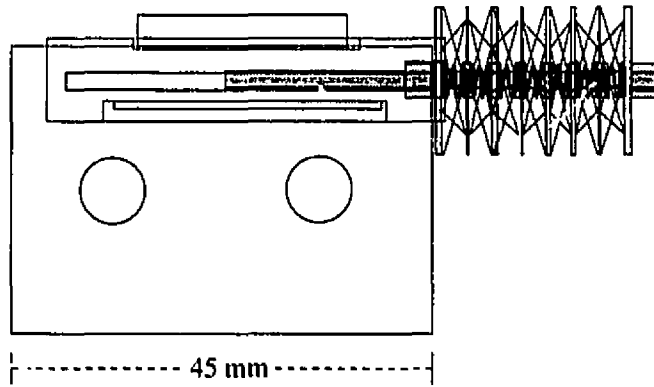
Some additional support structure is needed in order to integrate all of the camera platform's components. The actuator/sensor packages are held by the housing shown in Figure 5.10. Only one of the four actuators is shown for simplicity. This housing also provides support for the wiring needed to connect the actuators.

The components of the housing are clamped together by screws that compress the sensors. Two additional support beams are needed to connect the sensor/actuator pack to the paddles and finally to the gimbal. Figure 5.12 shows the complete integrated unit.

Each motion of the camera corresponds to differential motion of the actuators offering a path toward adapting the switching controller described earlier to the entire system. At present the camera is only actuated in an open loop fashion. The three motions, pan, tilt and torsion, are considered decoupled. For example, in order to tilt right the two actuators on the right side are turned on, pulling against the passive two actuators on the left side. Torsion is achieved by actuating two actuators on the diagonal. This can be seen in Figure 5.11 where the shaded actuators are contracting upon operation. Some preliminary results using this open loop scheme are given in the conclusions in Chapter six.

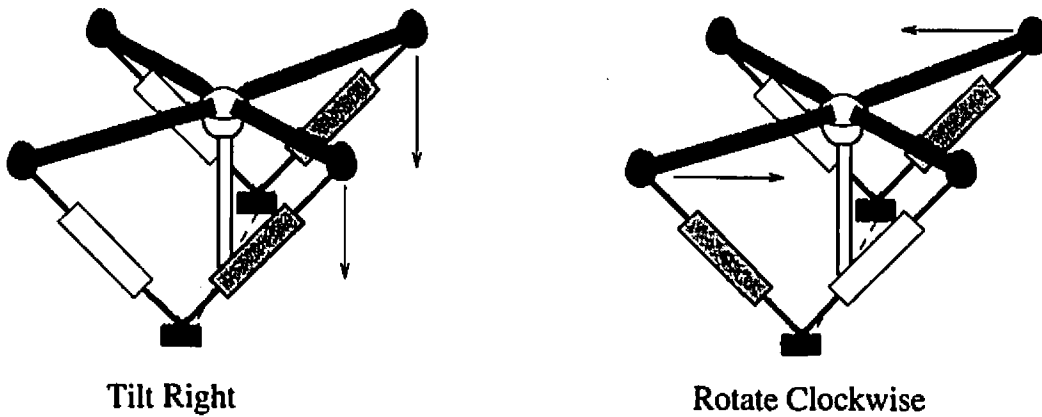


Front View



Side View

FIGURE 5.10. Sensor actuator housing

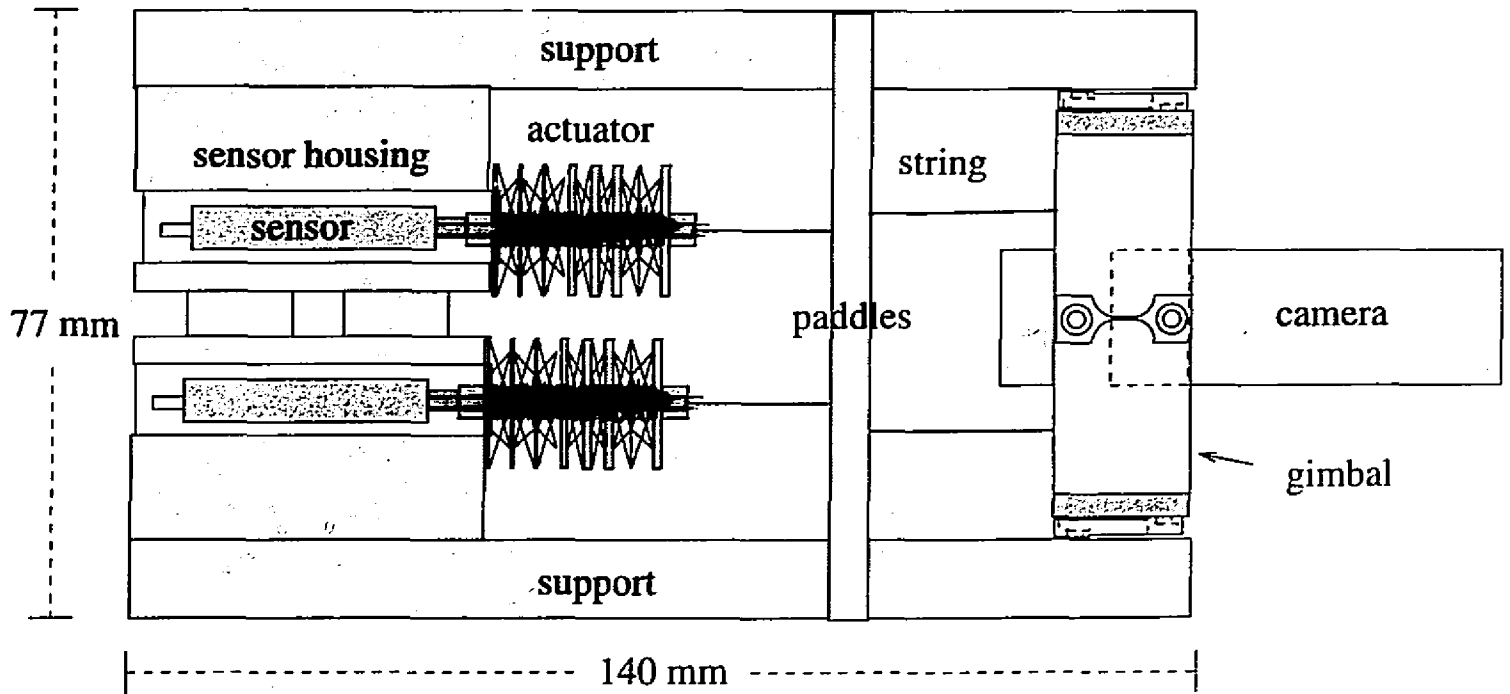


Tilt Right

Rotate Clockwise

FIGURE 5.11. Gimble motions

FIGURE 5.12. Integration of components



CHAPTER 6

Conclusions

1. Conclusions

A novel actuator using shape memory alloys has been proposed that overcomes two of the main drawbacks of shape memory alloys, those being limited strain and limited cycle lifetime. The abundant force available with SMA fibers is efficiently transformed to increase displacement by weaving the fibers in a double helix around supporting disks. This can also provide increased lifetime as the fibers can now be operated at lower than absolute percent strain.

An actuator prototype (see Figure 6.1) has been constructed with the following properties:



FIGURE 6.1. Shape memory alloy actuator

- light weight - 6 grams,
- compact - 17 mm cylinder, 25 mm long,
- powerful - 3.5 newtons,

- direct drive actuator,
- requires no gears or lubrication,
- elastic - smooth movements,
- acoustically silent,
- modular and
- inexpensive and simple construction.

Open loop experiments have been conducted to demonstrate the intrinsic properties of the actuator. Several two stage switching controllers were then applied to the actuator. The controller is based on a simple concept and produces satisfactory results. By adjusting the control gains it is possible to reach a set point with a small steady state error or to go into a desirable limit cycle within a specified limit. The two stage constant controller demonstrated that the added complexity of a linear proportional controller is not required, as similar results are obtained with the two stage constant magnitude controller which can be implemented in practice with very few electronic components.

A compact pan, tilt, and torsion camera unit was also constructed implementing the actuators to demonstrate their feasibility in a miniature application (see Figure 6.2).

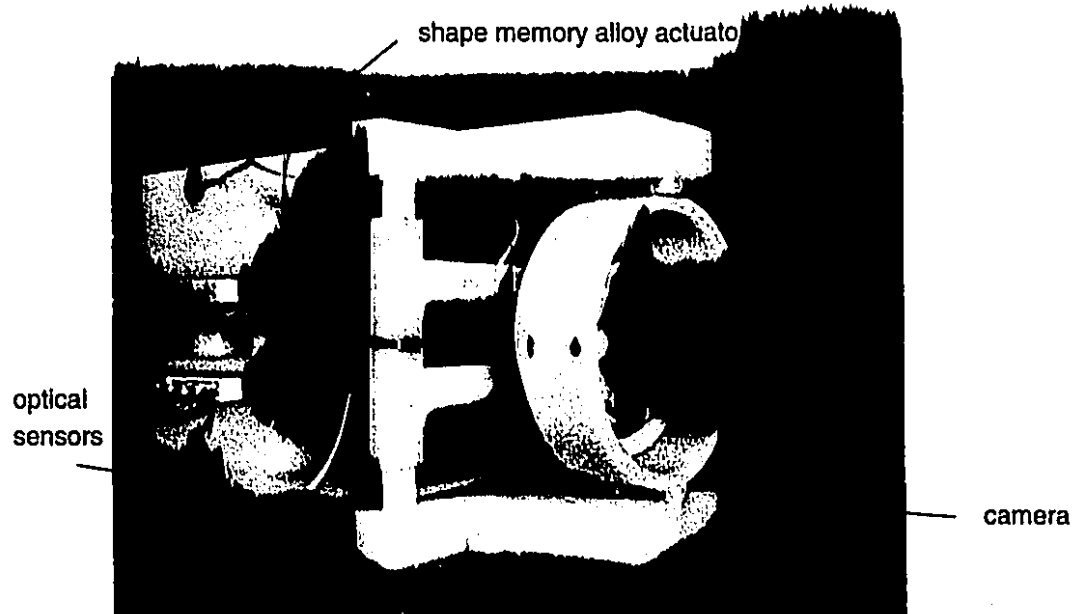


FIGURE 6.2. Camera prototype

This first camera prototype has the following preliminary characteristics:

- speed = 350 degrees/s

- acceleration = 5800 degrees/s²
- size = 180 mm x 77 mm x 77 mm
- Weight
 - camera = 50 grams
 - actuators = 24 grams
 - sensors = 25 grams
 - support structure = 250 grams
 - total weight = 349 grams

1.1. Future work. As with the design and construction of any prototype the door is opened for numerous future improvements and developments, ranging from the materials used to the actuators intended application.

The fibers in the actuator prototype were electrically connected in parallel. Given the low resistance of the NiTi, a large current at a low voltage was required in order to heat the fibers. A simple solution to this is to electrically connect the fiber in series [8]. This would be a simple matter for the actuator prototype, as a long single fiber was used in the construction. The double benefit of reducing the required current and increasing the applied voltage would then be realized.

More freedom of control over the motion of the actuators can be achieved by connecting the individual fibers electrically, either across individual cells or across the entire actuator. The individual fibers could then be scheduled to produce tentacle like motions. They could also be heated in a recruitment pattern similar to actual muscle fibers. In the recruitment method the number of fibers activated would depend on the force required. For example, if a low force is desired three or six of the fibers could be activated. If the entire force is needed all twelve will be activated. This would be useful in the controllers discussed in Chapter four in an effort to balance out the limit cycles.

Improvements in the response of the actuator can easily be realized by using the numerous forms of heat sinks. Considering the compact size and configuration of the actuator, it is not hard to imagine a flexible outer shell that could be used to contain a liquid coolant. The aluminium supporting disks could also be easily replaced with ceramic disks or high temperature plastic disks to alleviate the problems of uneven heating and wear along the notches. Finally with the intentions of an integrated mechatronic device, the resistance-position relationship of the SMA alloys could be utilized to provide internal position sensing [31].

APPENDIX A

Properties of NiTi

Flexinol is the trade name of the shape memory alloy used in the fabrication of the actuators in this thesis. The following property specifications was taken from [20].

Nickel-Titanium Alloy Physical Properties

- Density - 6.45 gr/cm
- Specific heat - 6-8 cal(mol.C)
- Melting point - 1250 C
- Thermal conductivity - 0.05 cal(cm-C-sec)
- Thermal expansion coefficient
 - Martensite - $6.6 \times 10^{-6}/C$
 - Austnite - $11.0 \times 10^{-6}/C$
- Electrical Linear Resistivity - 150 σ/m

APPENDIX B

Weave Patterns

As noted in chapter three, the actuator prototype is only one example of the weave patterns available. Both the number of notches and the offset angle, γ , determine the weave pattern. Examples of the weave pattern for the configurations detailed in table 1 will be shown in this Appendix. Most of the weave patterns can be achieved by weaving a single fiber back and forth between the end disks. The exceptions are noted in the following figures. As an additional note, the four notch actuator with an offset angle of 90° requires an even number of cells.

APPENDIX B. WEAVE PATTERNS

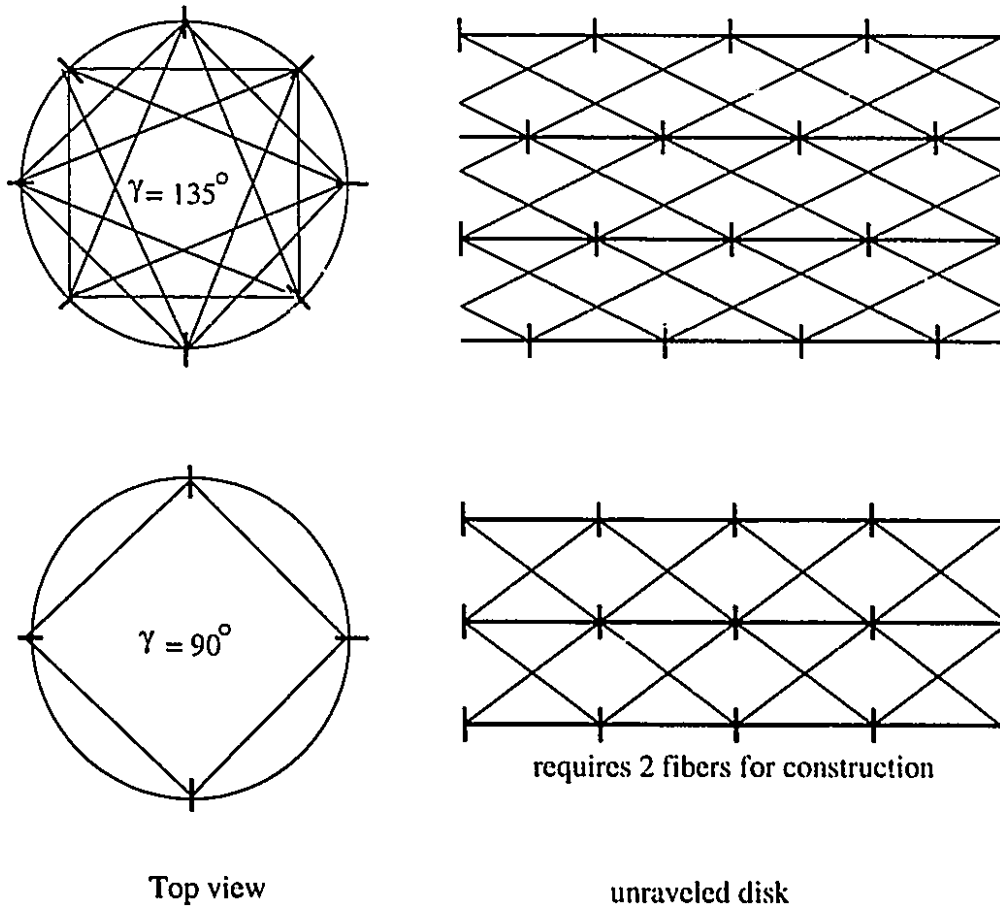
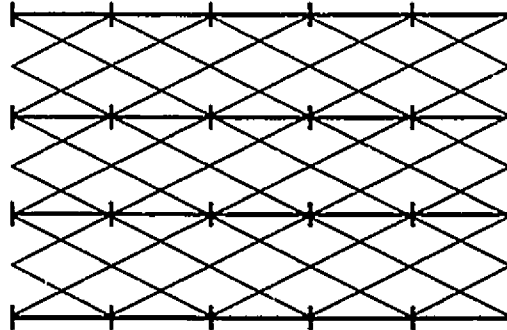
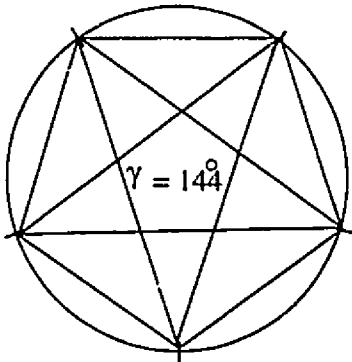
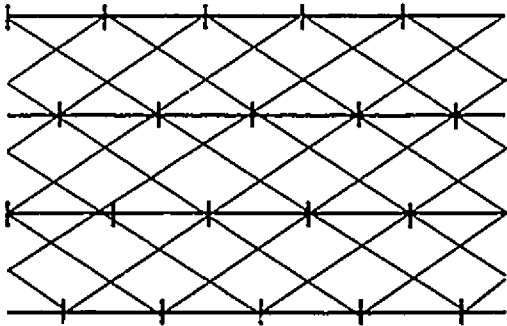
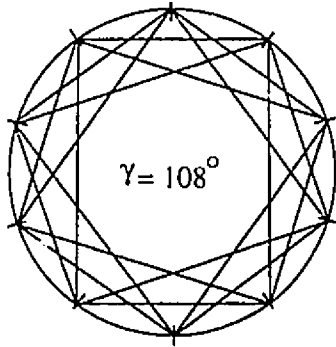


FIGURE B.1. Weave Pattern: 4 - notchs



Top view

Unraveled disk

FIGURE B.2. Weave Pattern: 5 - notchs

APPENDIX B. WEAVE PATTERNS

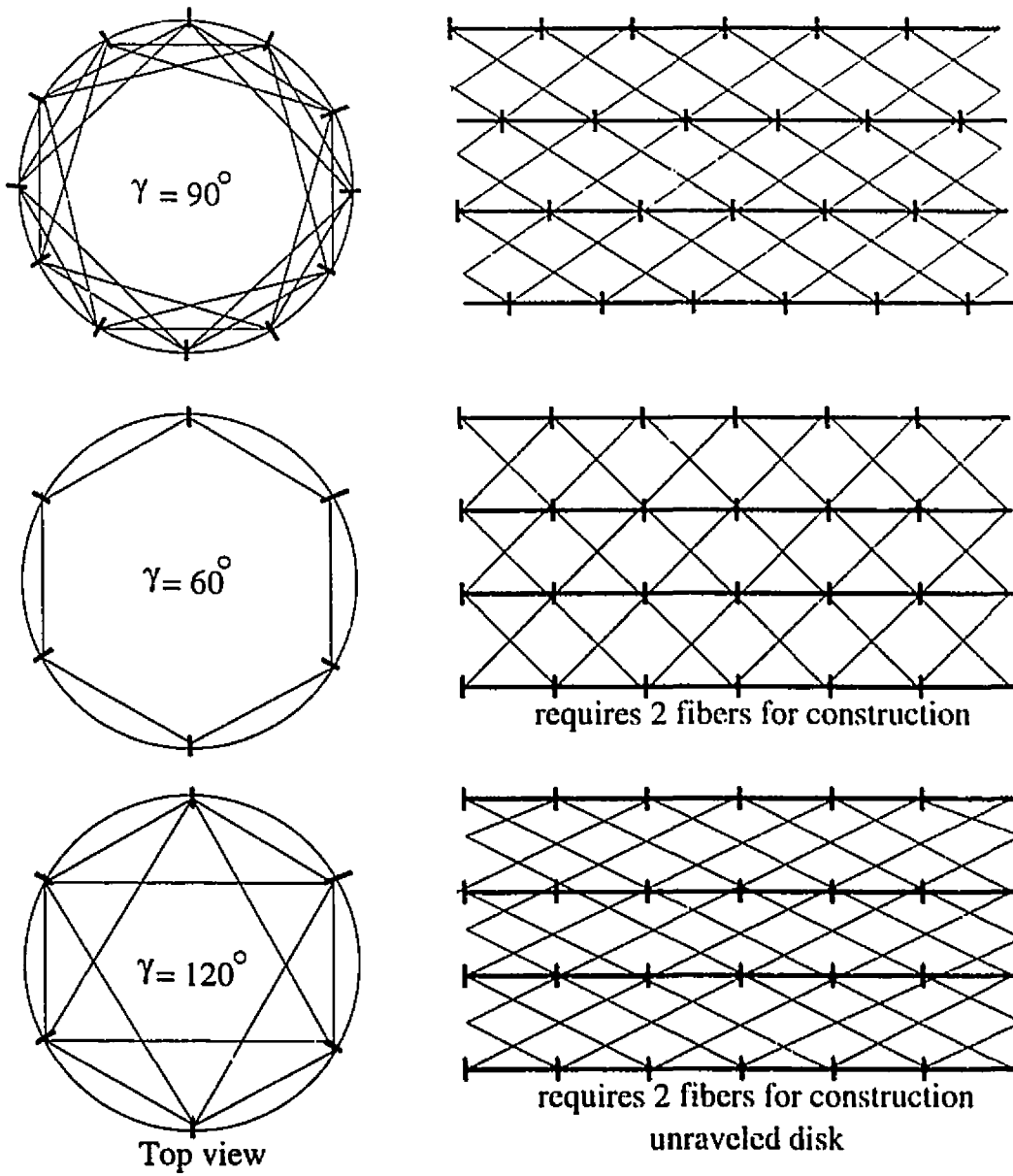
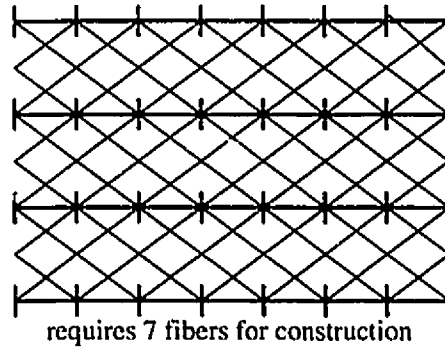
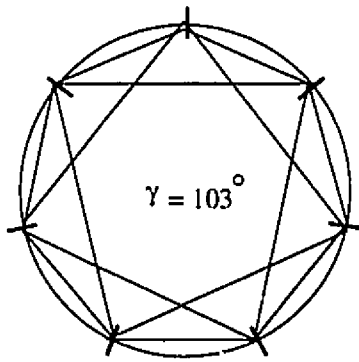
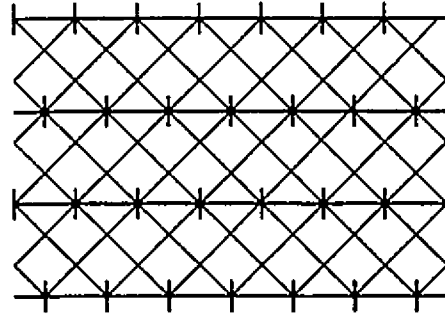
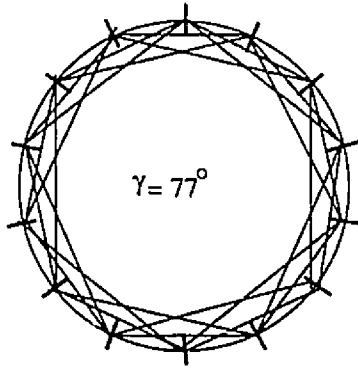


FIGURE B.3. Weave Pattern: 6 - notchs

APPENDIX B. WEAVE PATTERNS



Top view

unraveled disk

FIGURE B.4. Weave Pattern: 7 - notches

APPENDIX B. WEAVE PATTERNS

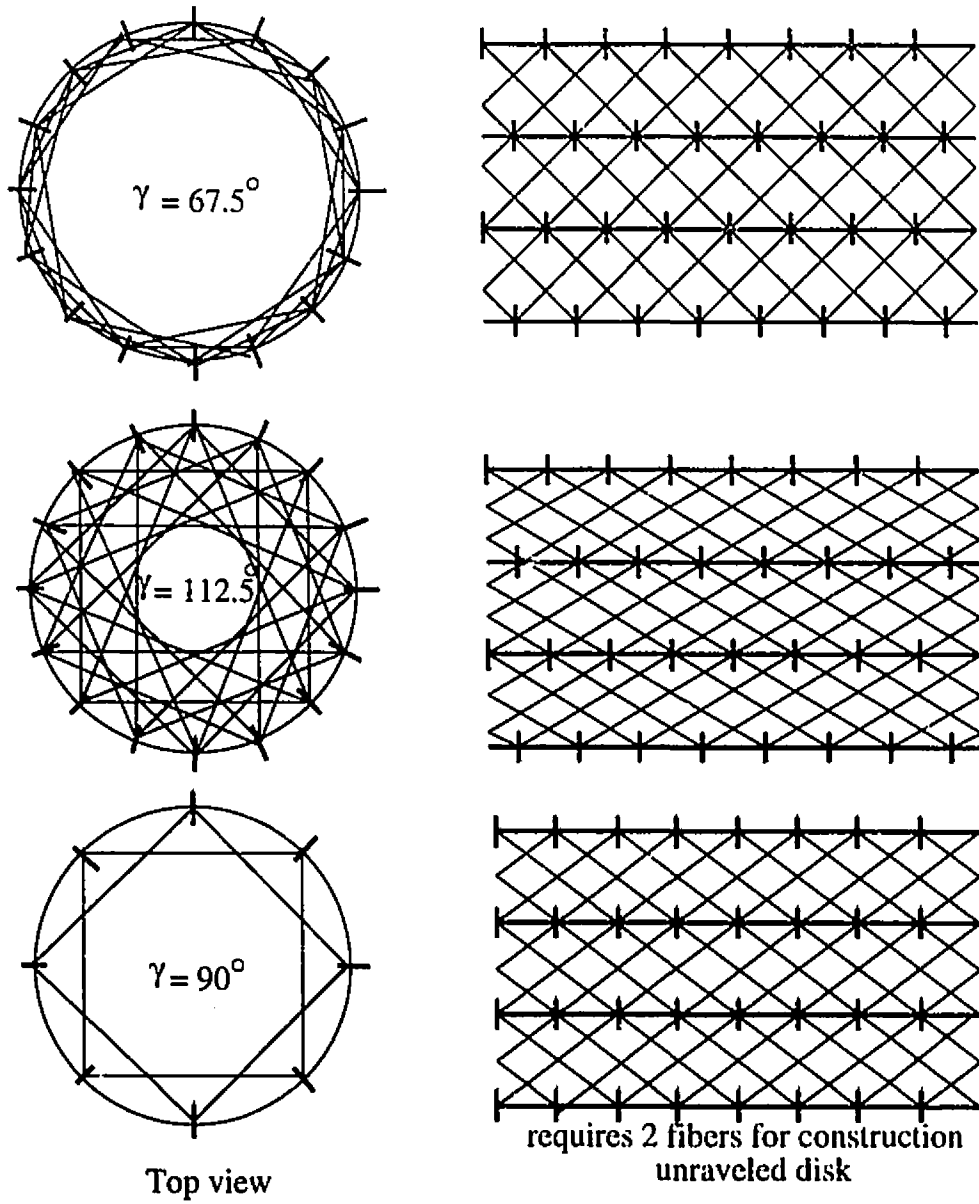


FIGURE B.5. Weave Pattern: 8 - notchs

REFERENCES

- [1] A. L. Abbot and N. Ahuja. Active surface reconstruction by integrating focus, vergence, stereo, and camera calibration. In *Third International Conference on Computer Vision*, pages 489-492, Osaka, Japan, 1990.
- [2] R. Bajcsy. Active perception. In *Proceedings of the IEEE*, volume 76, pages 966-1005, Jan 1988.
- [3] J.W. Ballantyne. Simple scaling laws for permanent magnet motors. *Spar J. of Engineering and Technology*, 2(1):50-57, 1993.
- [4] D.H. Ballard. Animate vision. *Artificial Intelligence*, 48:57-86, 1991.
- [5] Bederson, Wallace, and Schwartz. A miniature pan-tilt actuator: The spherical pointing mirror. *IEEE Transactions on Robotics and Automation*, 10(3):292-308, June 1994.
- [6] Marc Bolduc and Martin D. Levine. A foveated retina system for robotic vision. In *Proceedings of Vision Interface 1994, Banff, Alberta, Canada*, pages 1-8, 1994.
- [7] J.J Clark and N.J. Ferrier. Modal control of an attentive vision system. In *Third International Conference on Computer Vision*, pages 512-523, 1988.
- [8] P. Dario, M. Vergamascio, and L. Bicchi. A shape memory alloy actuating module for fine manipulation. In *IEEE Micro Robots and Teleoperator Workshop*, Hyannis, Ma, Nov 9-11 1987. IEEE Robotics and Automation council.
- [9] D. Yang, G. Lin, and R. Warrington. A computational model of shape memory alloys for the design and control of micro-actuators. *Micromechanical Systems*, v4, 1992.
- [10] T. Poggio et al. The mit vision machine. In *DARPA Image Understanding Workshop*, pages 177-198, 1988.
- [11] Buckminster Fuller. *Inventions: The Patented Work of Buckminster Fuller*. St. Martin's Press, Toronto, 1983.
- [12] John E. Gibson. *Nonlinear Automatic Control*. McGraw-Hill Inc., 1963.
- [13] C. Gosselin and J.F. Hamel. The agile eye: a high-performance three-degree-of-freedom camera-orienting device. In *IEEE International Conference on Robotics and Automation*, volume 1, pages 781-786, San Diego, May 1994.
- [14] M. Hashimoto, Mansanori Takeda, Hirofumi Sagawa, and Ichiro Chiba. Application of shape memory alloy to robotic actuators. *Journal of Robotic Systems*, 2(1):3-25, 1985.
- [15] Vincent Hayward. Design of hydraulic robot shoulder based on combinatorial mechanism. *Experimental Robotics 3*, 1993.
- [16] Dai Honma, Yoshiyuki Miwa, and Nobuhiro Iguchi. Micro robots and micro mechanisms using shape memory alloy. In *Integrated Micro Motion Systems, Micro-machining, Control and Application*, Nissin, Aichi, Japan, Oct. 1989. The Third Toyota conference.
- [17] Ian Hunter, Serge Lafontaine, John Hollerbach, and Peter Hunter. Fast reversible NiTi fibers for use in microrobotics. In *Microelectro-mechanical Systems*, Nara, Japan, Jan 1991.

- [18] Koji Ikuta. Micro/miniature shape memory alloy actuator. In *IEEE Robotics and Automation Society*, volume 3, pages 2156-2161, Los Alamitos, California, May 1990. IEEE Computer Society Press.
- [19] Koji Ikuta, Masahiro Tsukamoto, and Shigeo Hirose. Mathematical model and experimental verification of shape memory alloy for designing micro actuator. In *Proceedings of the IEEE MicroElectroMechanical Systems Conference*, pages 103-108, 1991.
- [20] Dynalloy Inc. Technical characteristics of flexinol actuator wires. brochure, Irvine, CA 92715.
- [21] M. Jenkin, E. Milios, and J. Tsotsos. TRISH : the Toronto-IRIS stereo head. *Machine Vision and Robotics*, 1708:36-46, 1992.
- [22] Katsutoshi Kuribayashi. A new actuator of a joint mechanism using TiNi alloy wire. *The International Journal of Robotics Research*, 4(4), 1986.
- [23] Katsutoshi Kuribayashi. Millimeter size joint actuator using shape memory alloy. In *The IEEE MEMS*, Salt Lake City, Feb 1989.
- [24] Ronald L. Kurtz. Kinematic and optimization of a parallel robotic wrist mechanism with redundancy. Master's thesis, McGill university, Montreal Quebec, Jan 1990.
- [25] Vadim I. Utkin. *Sliding Modes in Control Optimization*. Springer-Verlag, 1992.
- [26] Li and Slotine. *Applied Non-Linear Control*. Prentice Hall, 1991.
- [27] Daniel Richard Madill. Modelling and stability of a shape memory alloy position control system. Master's thesis, Applied Science, University of Waterloo, 1993.
- [28] K. Pahlavan and J.O. Eklund. A head-eye system for active, purposive active vision. TRITA-NA-9031.
- [29] Dominiek Reynaerts and Hendrik Van Brussel. Development of a SMA high performance robotic actuator. In *Fifth International Conference on Advanced Robotics*, volume 2, pages 19-27, New York, NY, 1991.
- [30] M. Swain and M. Stricker, editors. *Promising Directions in Active Vision*, University of Chicago, August 1991.
- [31] Masanori Takeda, Minoru Hashimoto, and Kimiko Sato. A new displacement sensor using psuesoelastic titanium-nickel alloy wire. *Journal of Robotic Systems*, 3(4):441-459, 1986.
- [32] Toki Corporation, Tokyo, Japan. *Biometal Guidebook*, 1987.
- [33] James A. Walker. A small rotary actuator based on torsionally strained SMA. In *IEEE Micro Robots and Teleoperator Workshop*, Hyannis, Ma, Nov9-11 1987. IEEE Robotics and Automation council.
- [34] A.J. Wavering, J.C. Fiala, K.J. Roberts, and R. Lumia. Triclops: A high-performance trinocular active vision system. In *IEEE Int. Conf. on Robotics and Automation*, pages 410-41, 1993.

Document Log:

Manuscript Version 0
Typeset by $\mathcal{A}\mathcal{M}\mathcal{S}\text{-}\mathcal{L}\mathcal{A}\mathcal{T}\mathcal{E}\mathcal{X}$ -- 7 February 1995

DANNY GRANT

CENTER FOR INTELLIGENT MACHINES, MCGILL UNIVERSITY, 3480 UNIVERSITY ST., MONTRÉAL (QUÉBEC) H3A
2A7, CANADA,
E-mail address: grant@cim.mcgill.ca

Typeset by $\mathcal{A}\mathcal{M}\mathcal{S}\text{-}\mathcal{L}\mathcal{A}\mathcal{T}\mathcal{E}\mathcal{X}$